

**MODELLING OF ELECTRON BEAM DEFLECTION SYSTEM FOR BEAM
POSITION CONTROL IN METAL ADDITIVE MANUFACTURING**

by

Scott Parks

B.Sc.E., Queen's University, 2016

B.A., Queen's University, 2016

A THESIS SUBMITTED IN PARTIAL FULFILLMENT OF
THE REQUIREMENTS FOR THE DEGREE OF

MASTER OF APPLIED SCIENCE

in

THE FACULTY OF GRADUATE AND POSTDOCTORAL STUDIES
(Mechanical Engineering)

THE UNIVERSITY OF BRITISH COLUMBIA
(Vancouver)

April 2020

© Scott Parks, 2020

The following individuals certify that they have read, and recommend to the Faculty of Graduate and Postdoctoral Studies for acceptance, a thesis entitled:

Modelling of Electron Beam Deflection System for Beam Position Control in Additive Manufacturing

submitted by Scott Parks in partial fulfillment of the requirements for

the degree of Master of Applied Science

in Mechanical Engineering

Examining Committee:

Dr. Yusuf Altintas, Mechanical Engineering
Supervisor

Dr. Chadwick Sinclair, Materials Engineering
Supervisory Committee Member

Dr. Minkyun Noh, Mechanical Engineering
Supervisory Committee Member

Abstract

Additive manufacturing (AM) is a layer-based process for producing parts. Metal AM is an attractive technology for the aerospace and biomedical industries due to its ability to produce complex geometries from difficult to cut materials. Electron beam melting (EBM) is a form of metal AM, which uses an electron beam to melt metal powders into fully dense parts. The position and velocity of the electron beam are important parameters in determining the success of production in EBM. In order to provide robust control of the beam position, a model for real-time prediction of the electron beam position has been developed.

The electron beam's position is controlled by an electron beam deflection system, which uses electromagnetic poles to deflect the beam to a desired position on the build plate. This thesis presents an electron beam deflection system model, which can predict the beam position during EBM operation. The current behavior within the deflection coils is modelled using an equivalent circuit to determine the effective current within the coils. The prediction of the magnetic flux density distribution generated by the coils based on the effective current in the coils is described. The interaction between the generated magnetic flux density and the electron beam gun structure is modelled as a first order system, to predict the lag induced by eddy currents on the beam's position. With the magnetic flux density distribution, the position of the electron beam was predicted using a discrete-time domain simulation. Crosstalk between the axes of the system was modelled with an empirical model. The proposed model was validated through FEM simulations and experimentation on a single-axis prototype as well as an EBM machine.

Recommendations for hardware alterations within the EBM machine are made, which would reduce error in the beam's position. Additionally, a pole-zero cancellation controller is designed to compensate for errors caused by eddy currents. A feed forward controller is designed, which predicts the crosstalk between the system's axes and compensates for the error in real-time.

Lay Summary

Additive manufacturing (AM) is a process for producing parts in a layer-by-layer method. AM with metals is an attractive technology for its versatility in producing complex geometries out of difficult to cut materials. Electron beam melting (EBM) is an AM technology that utilizes a high-power electron beam to melt metal powder into fully dense solid parts. Commercial EBM machines have a high cost and high failure rates for producing parts. For EBM to become more economically viable and accurate, investigations into the control of the EBM machines must be conducted. An important aspect in the EBM process is the electron beam's position and velocity, which is controlled by an electron beam deflection system. This thesis presents and validates a dynamic model of the electron beam deflection system, which may be utilized in the development of more robust control of the electron beam's position and velocity.

Preface

I was the lead investigator for the work presented in Chapters 3, 4 and 5. I planned the experimental design, conducted experimentation, and completed the analysis of results. Ralf Edinger of Canmora Inc. aided in the conduction of experiments within the Canmora EBM machine. Dr. Yusuf Altintas was the academic supervisor.

Ralf Edinger, and Canmora Inc. designed and supplied the deflection coils and beam columns used for experiments external to the EBM machine. The deflection coils are designed for the updated Canmora deflection system. Further, Canmora provided a fixture to secure the experimental build plates within the EBM machine.

A version of chapter 3 and chapter 5 have been presented at a conference. I presented the material at the NSERC Holistic Innovation in Additive Manufacturing (HI-AM) 2nd conference. The manuscript “Modelling of Electron-beam Deflection System” was written by Scott Parks, Z. Murat Kilic, and Yusuf Altintas.

Table of Contents

Abstract.....	iii
Lay Summary	v
Preface.....	vi
Table of Contents	vii
List of Tables	x
List of Figures.....	xi
List of Symbols	xiv
List of Abbreviations	xviii
Acknowledgements	xix
Chapter 1: Introduction	1
Chapter 2: Literature Review.....	8
2.1 EBM Process Control	8
2.2 Control of Electron Beam Deflection	9
2.3 Summary.....	11
Chapter 3: Model of Electron Beam Gun.....	12
3.1 Electron Gun	12
3.1.1 Cathode	14
3.1.2 Bias Cup.....	14
3.1.3 Anode.....	15
3.2 Astigmatism System	18
3.3 Focusing System	18

3.4	Deflection System.....	19
3.4.1	Current Amplifier.....	21
3.4.2	Deflection coil.....	22
3.4.2.1	Deflection Coil Equivalent Circuit	22
3.4.2.1.1	Skin Effect.....	24
3.4.2.1.2	Proximity Effect	25
3.4.2.2	Magnetic Flux Density Generation.....	26
3.4.3	Beam Column	29
3.4.4	Electron Deflection.....	30
3.4.5	Crosstalk	34
3.5	Summary.....	35
Chapter 4: Position Control of Electron Beam		38
4.1	Open-Loop Eddy Current Compensation	38
4.2	Feed forward Crosstalk Compensation.....	41
Chapter 5: Simulation and Experimental Validation.....		43
5.1	Simulation and Experimental Setups	43
5.1.1	Single-Axis Test Setup	44
5.1.1.1	FEM Simulation Setup.....	44
5.1.1.2	Single-Axis Test Setup	45
5.1.2	Two-Axis Canmore EBM Machine	49
5.2	Results.....	52
5.2.1	Coil Voltage Response.....	52
5.2.1.1	Single-Axis Deflection System.....	52

5.2.2	Magnetic Flux Density Distribution	55
5.2.2.1	Single-Axis Test Setup	55
5.2.3	Beam Column Dynamic Response	56
5.2.3.1	Single-Axis Test Setup	57
5.2.3.1.1	Open-Loop Eddy Current Compensation on Single-Axis Test Setup	59
5.2.3.2	Two-Axis Canmora EBM.....	60
5.2.4	Electron Beam Deflection.....	63
5.2.4.1	Single-Axis Deflection System.....	63
5.2.4.2	Two-Axis Canmora EBM.....	65
5.2.5	Crosstalk Response and Compensation	66
5.2.5.1	Two-Axis Canmora EBM.....	66
5.3	Summary	70
Chapter 6: Conclusion.....		72
6.1	Future Directions	73
Bibliography		75

List of Tables

Table 5.1: Measured DC-resistance, self-inductance, and parasitic capacitance of the external deflection coils.....	54
Table 5.2: Summary of simulated and measured time constants of beam column stage ($B(j\omega)B_{coil}(j\omega)$).....	62

List of Figures

Figure 1.1: Steps of the EBM process	5
Figure 1.2: Example of two systems with varying bandwidth responding to sudden changes in commanded position.	7
Figure 3.1: Diagram of electron beam gun components.....	12
Figure 3.2: Diagram of electron beam gun with potential differences between the three components represented by a simple circuit diagram.	13
Figure 3.3: Effect of accelerating voltage on electron velocity and Lorentz factor.	17
Figure 3.4: (a) Diagram of electron beam deflection system. (b) Top view of electron-beam deflection system.	20
Figure 3.5: Block diagram of two-axis beam deflection system. Units: Current [A], magnetic flux density [T: Tesla = 10^4 Gauss].....	20
Figure 3.6: (a) Equivalent circuit of multi-layer air coil. (b) Alternative equivalent circuit of multi-layer air coil with parasitic capacitance neglected.....	22
Figure 3.7: Skin effect in a circular conductor.	24
Figure 3.8: Signal frequency's effect on skin depth for a copper conductor.....	25
Figure 3.9: Proximity effect in conductor bundle.....	26
Figure 3.10: Side and front view of discretization of Biot-Savart Law for multi-layer air coil ...	28
Figure 3.11 : Vector of electron beam velocity with angles of deflection shown.	31
Figure 4.1: Block diagram of a single-axis deflection system with pole cancellation controller.	39
Figure 4.2: Example bode plot for designed pole-zero cancellation controller.....	40

Figure 4.3: Block diagram of two-axis deflection system with feed forward crosstalk compensation.	41
Figure 5.1: FEM model of beam deflection system.....	45
Figure 5.2: Diagram and photograph of external single-axis deflection system.	46
Figure 5.3: Linear amplifier used to provide current to external deflection coils.	47
Figure 5.4: Experimental circuit for measurement of deflection coil self-resonant frequency. ...	49
Figure 5.5: Canmora EBM machine vacuum chamber.....	50
Figure 5.6: Passive low-pass filter implemented on voltage input signal.....	51
Figure 5.7: Measured FRF of voltage input filter.	51
Figure 5.8: FRF of deflection coils impedance.....	53
Figure 5.9: Step response of deflection coil with large resistor connected in series.	54
Figure 5.10: Predicted, simulated, and measured magnetic flux density distribution along system axes.	56
Figure 5.11: Simulated FRFs of beam column stage with various conductivities.....	58
Figure 5.12: Simulated and measured FRFs of beam column stage.....	59
Figure 5.13: FRF of beam column stage with open-loop compensation.	60
Figure 5.14: Melt pools from single-axis frequency sweeps experiments. a) x-axis, b) y-axis....	61
Figure 5.15: Simulated and measured FRFs of beam column stage.....	62
Figure 5.16: Deflection output (x, or y) for varying current input (I_s) amplitudes.	63
Figure 5.17: Deflection output (x_{nom}) for varying accelerating voltages (VA).	64
Figure 5.18: Melt pools from static currents of $I_S = -1A$ to $I_S = 1A$	65
Figure 5.19: Deflection output (x, or y) for varying current input (I_s) amplitudes.	66
Figure 5.20: Resulting melt pool from angular sweep of Canmora deflection system.....	67

Figure 5.21: Simulink model of electron beam deflection system, used for calibration of crosstalk parameters 68

Figure 5.22: Output of Simulink simulated open-loop deflection system a) x-axis frequency sweep, b) y-axis frequency sweep, c) two-axis angular sweep..... 69

Figure 5.23: Experimental output for beam deflection system with feed forward compensation of crosstalk. a) x-axis frequency sweep, b) two-axis angular sweep 70

Figure 5.24: Simplified block diagram of deflection system representing the measured response. 71

List of Symbols

P_{beam}	Electron beam power
I_{beam}	Electron beam current
V_A	Accelerating current
PE_e	Electric potential energy of electrons
KE_e	Kinetic energy of electrons
q	Charge of an electron
γ	Lorentz Factor
v_0	Magnitude of the velocity of electron beam
c	Speed of light
m_e	Rest mass of electrons
$\begin{bmatrix} G_{CT,xx}(s) & G_{CT,xy}(s) \\ G_{CT,yx}(s) & G_{CT,yy}(s) \end{bmatrix}$	Transfer functions of crosstalk between x- and y- axes
$G_{DC}(s)$	Transfer function of deflection coil
$G_{BC}(s)$	Transfer function of beam column
V_{in}	Voltage input signal into power amplifier
K_{PA}	Voltage to current gain of power amplifier
I_S	Current output of power amplifier
I_{coil}	Current passing through inductor
I_{loss}	Current loss through parasitic capacitance
L_{coil}	Self-inductance of deflection coils

R_{coil}	DC-resistance of deflection coils
$\omega_{n,DC}$	Self-resonant frequency of deflection coils
C_p	Parasitic capacitance of deflection coils
α_{CT}	Crosstalk gain parameter
τ_{CT}	Crosstalk time constant parameter
V_S	Voltage supplied by current amplifier
s	Laplace operator
ω	Frequency of signal in rad/s
$K_{B;(x,y,z)}$	Distributed current to magnetic flux density gain
$B_{coil;(x,y,z)}$	Distributed magnetic flux density generated by deflection coils
τ	Time constant of beam column
$B_{(x,y,z)}$	Distributed magnetic flux density after eddy current losses
K_d	Magnetic flux density to deflection distance gain
$\Phi(s)$	Transfer function of crosstalk between the system axes
x_{nom}	Nominal beam position in the x-direction
y_{nom}	Nominal beam position in the y-direction
x_{CT}	Beam position crosstalk error in the x-direction
y_{CT}	Beam position crosstalk error in the y-direction
x	Actual beam position in the x-direction
y	Actual beam position in the y-direction
δ	Skin depth of current signal in conductor
ρ	Resistivity of copper

f	Frequency of signal in Hz
μ_r	Relative permeability of material
μ_0	Permeability of free space
N	Number of windings in deflection coil
W	Width of the deflection coils
H	Height of the deflection coils
L	Length of the deflection coils
R	Radius of deflection coil corner
Δw	Width of discrete coil element
Δh	Height of discrete coil element
Δl	Length of discrete coil element
$\Delta\theta$	Angular size of discrete coil element
\mathbf{a}	Displacement vector from point in space to discrete coil element
$\mathbf{B}_{i;(x,y,z)}$	Magnetic flux density contribution of individual coil section
\mathbf{E}	Electrostatic field vector
$\mathbf{F} = \begin{Bmatrix} F_x \\ F_y \\ F_z \end{Bmatrix}$	Lorentz force on moving electron
$\mathbf{v} = \begin{Bmatrix} v_x \\ v_y \\ v_z \end{Bmatrix}$	Velocity vector of moving electron
$\mathbf{B} = \begin{Bmatrix} B_x \\ B_y \\ B_z \end{Bmatrix}$	Magnetic flux density vector
p_{eddy}	Pole produced by eddy currents within the beam column

z_c	Zero of pole-zero cancellation controller
p_c	Pole of pole-zero cancellation controller
$\Phi_{FF}(s)$	Fitted transfer function of crosstalk between the system axes
I_r	Reference current signal
e_I	Error signal in current control loop
K_{PI}	Proportional gain in current controller
ω_{II}	Break frequency of integral action of current controller
ω_c	Open-loop bandwidth of current controller
x_r	Reference position signal
e_x	Error signal in position control loop
K_x	Measured magnetic flux density to position gain
B_x	Measured magnetic flux density in position control loop
K_{Px}	Proportional gain in position controller
ω_{Ix}	Break frequency of integral action of position controller
α	Parameter of lead-lag controller
T	Parameter of lead-lag controller
R_{add}	Resistance added to deflection coil circuit
σ	Conductivity of beam column

List of Abbreviations

AM – Additive manufacturing

BW – Bandwidth

CAD – computer-aided design

DED – Direct energy deposition

EBM – Electron beam melting

FEM – Finite element method

FRF – Frequency response function

MMF – Magnetomotive force

NMRI – Nuclear magnetic resonance imaging

PI – Proportional integral controller

PID – Proportional integral derivative controller

SEM – Scanning electron microscope

SLM – Selective laser melting

Acknowledgements

I would like to express my gratitude to my supervisor Prof. Yusuf Altintas for his continued support and guidance throughout my time in the Manufacturing Automation Laboratory. I appreciate the confidence he placed in me when he accepted me into his lab and will use the lessons he taught me for the rest of my engineering career.

I would also like to thank Prof. Cockcroft, Prof. Maijer, and Prof. Sinclair for accepting me into the additive manufacturing group and providing my research with a meaningful goal.

I would also like to thank Ralf Edinger for his willingness to share his expertise and answer my questions, which elevated my understanding of EBM.

To my friends and peers in the Manufacturing Automation Laboratory, thank you for your technical and moral support throughout my time at UBC and thank you for all the shared laughs and perspectives. I would like to especially thank Murat Kilic for his guidance with my research, allowing me to feel confident in my decisions as a researcher.

Finally, I would like to thank my family whose constant encouragement reminded me that my time as student had a purpose beyond my coursework. To my Nana Mary Jean, I would like to thank you for convincing me that graduate studies was worth pursuing simply because I aspired for it. And to my partner Ellen, thank you so much your unending support and for continuing to show me how to face my challenges with optimism and determination.

Chapter 1: Introduction

Additive manufacturing (AM) is a layer-based process for producing parts in which material is selectively added to the part until the desired geometry is achieved. AM of metal parts is a desirable technology as it allows for the ease of manufacturing lightweight parts made of difficult to cut metals due to their poor thermal conductivity (e.g. Ti-6Al-4V, stainless steel, nickel alloys, Inconel, etc.). Many of these materials have desirable properties for the aerospace and biomechanical industries. Therefore, there exists an industrial interest in the development of metal AM technologies. The layer-by-layer AM process allows for more flexibility in build geometry, including the potential to generate parts with freeform surfaces and internal structures. This flexibility in build geometry when used in tandem with finite element method (FEM) based mass optimization allows for parts with a high strength-to-weight ratio, which is also desirable in many aerospace and biomechanical parts. Future developments in metal AM include the utilization of multiple materials for a single part, such that various mechanical properties can be achieved in different segments of a part [1]. Additionally, with the control of a metal's heating and cooling, the microstructure of the material can be optimized in each segment of a part, such that fine adjustment of mechanical properties can be achieved [2]. With the additional degrees of freedom of mechanical properties afforded by AM, it is important that the process window of the machines are as large as possible, such that process designers are able to utilize all the benefits of AM. Broadening the AM machine process window requires a deep understanding of the machine operation such that parameters may be precisely controlled.

Another benefit to AM is the rapid prototyping capabilities. Due to the layer-based nature of the AM process, the generation of machine code is simplified to a series of 2D planes with no tool changes, which can be generated much more rapidly than 3D or 5D machine codes. Additionally, versatility in the machine parameters means that no alterations to the machines are required for different builds. Therefore, customization of part geometry is simply achieved by altering the part's computer-aided design (CAD) model. This rapid customization of parts is an attractive quality for the biomechanical industry, as orthopedics can be customized for each patient increasing biocompatibility [3].

Metal AM processes are grossly categorized by heat source (e.g. laser or electron beam) and feed stock deposition (e.g. powder bed, direct powder deposition, and wire fed). Electron beam heat sources have a few major benefits over laser. The electron beam's position is controlled via an electromagnetic system, whereas lasers typically utilize a mirror array system. This lack of mechanical parts in the beam position control allows for faster position response times, thereby broadening the process window of electron beam heat sources. Electron beam sources require an ultra-high vacuum, as the electron beam is unable to travel in a gas filled environment without scattering. This ultra-high vacuum decreases the material cooling rates in electron beam AM reducing the residual stresses within parts [4]. However, generating the necessary vacuum greatly increases the capital and operating costs as well as the complexity of electron beam AM machines. Due to the electrically charged nature of electron beam heat sources, the heat source is unable to interact with magnetic materials without significant lensing effects, limiting the potential applications of the technology. An issue experienced by electron beam heat sources is the phenomenon known as smoking. Smoking is the name given to the rapid dissipation of metal

powder caused by the buildup of negative charge on the surface of the powdered substrate. The buildup of charge on the powder particles creates an inter-particle repelling force, which overcomes the gravitational force holding the particles to the build plate, causing them to dissipate. Any occurrence of smoking during the metal AM process will cause the entire part production to fail, thus it is critical that smoking is avoided. It has previously been demonstrated that the buildup of charge occurs due to the dielectric oxide covering the surface of the powder particles, which creates a capacitance that the charge in the beam must travel through before reaching ground. The common method for avoiding smoking is to heat the powder substrate until sintering between the particles occurs, increasing the force required to cause smoking. This preheating of the powder is an additional step in the electron beam AM process, which increases the build time and cost of any part [5].

Selective laser melting (SLM) and electron beam melting (EBM) both utilize powder bed deposition for metal AM. Powder bed deposition is conducted by depositing a complete layer of powder for each layer of the print, whereas direct energy deposition (DED) and wire fed deposition selectively deposits material only in the necessary locations. Powder bed deposition simplifies the AM process as the deposition is identical for each layer. However, hollow structures are not possible without a method to remove the powder from the internal structure, and more powder is used during prints increasing the cost of part production.

This thesis will focus on the deflection system in the EBM process, that is, AM with an electron beam heat source and powder bed deposition system.

Once the machine code is uploaded to the EBM machine, the EBM process can be described as a repeating five step process, as shown in Figure 1.1. The first step of the EBM process is to preheat the previously printed layer, or if it is the first layer, preheat the build plate. Preheating temperatures suggested by EBM machine manufacturers are in the range of 600°C to 750°C [4]. For the preheating and reheating stages an unfocused low power beam is used, reducing the charge density on the part surface and avoiding the previously mentioned smoking phenomenon. This preheating stage is completed so that when the new layer of powder is deposited on the heated build plate, it will be heated to near sintering temperatures, avoiding smoking when the electron beam is applied. Once the substrate is adequately preheated, the new layer of powder is deposited. A common method for depositing a powder bed layer in AM processes is a rake system. The rake system pushes the powder from a hopper, where it is stored, over the entire build plate, smoothing the powder to a specified height as it travels. As the cool powder is raked over the previously preheated layer, the surface temperature of the part decreases. A raster scan of a low power unfocused electron beam is applied to the partially sintered layer, to completely sinter the new layer so that smoking is avoided during the melting stage of the process. Once complete sintering is achieved the cross-section of the part at the current layer height is melted into the newly deposited layer. The melt stage occurs in two parts, the outer profiles of the cross-section are melted in what is known as contour melting, then the inner area of the cross-section is melted in what is known as hatch melting. The hatch melt is usually completed as a raster scan, with the scan speed, and spacing between the hatch lines set by the machine user such that part porosity is minimized [6]. After the cross-section of the part has been melted, the build plate is lowered by a layer height increment, such that when next powder layer is deposited by the rake it is smoothed

at the correct height. This EBM process is repeated for each layer of the part until the final part height is achieved.

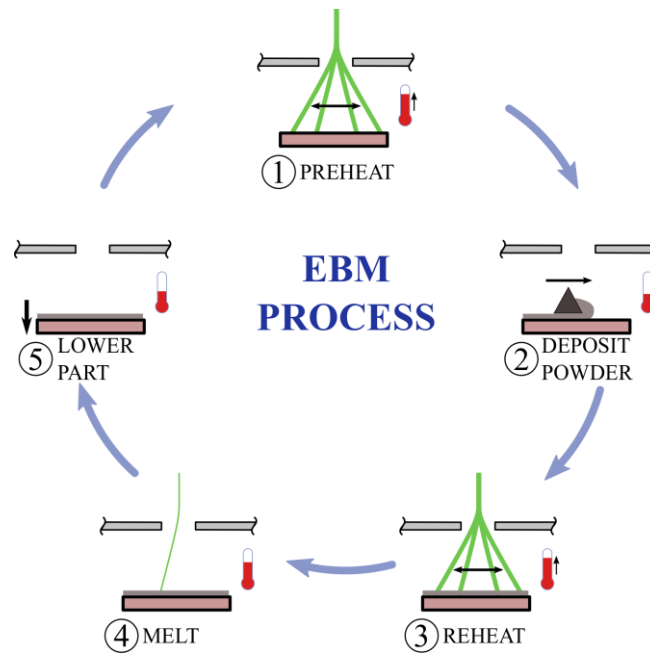


Figure 1.1: Steps of the EBM process

During the EBM process, the beam must be moved over the part surface. Since many EBM machines do not have the capability to modulate the beam power during operation, the energy input into the part is controlled by varying the beams tangential velocity. Therefore, the energy input can be reduced to near zero by increasing the beam velocity to very high speeds. This rapid movement is utilized to move the beam between melt pools. To achieve this rapid movement, the beam position control system should have a high bandwidth (e.g. above 5 kHz).

During the EBM process the electron beam position is controlled with an electron beam deflection system. The beam deflection system utilizes electromagnetic poles to induce a force on the electron beam, deflecting the beam to the desired position. It is desired that the beam follows a reference

path at a specified velocity with minimal trajectory errors. Errors occur when sudden position changes are commanded, due to the deflection system being unable to respond quickly enough. Beam trajectory errors can be either position or velocity errors. Position errors can create dimensional errors in the final part. Velocity errors cause a lack or excess of energy to be input into the part surface. This discrepancy between desired and actual energy input can create unstable melt pools or other errors in the finished part, such as porosity. Figure 1.2 shows an exaggerated example of two actual systems (red and blue), responding to sudden changes in commanded position (black), with position overshoot and velocity drops occurring at sudden right angles in reference position.

The bandwidth of the deflection system defines its responsiveness to sudden commands. The higher the systems bandwidth, the faster it is capable of responding to a sudden command, thereby reducing potential beam trajectory errors, as shown in the example in Figure 1.2. A system's bandwidth may be increased with a well-designed controller, or by applying changes to the system hardware that are found to inhibit the system's ability to respond quickly (e.g. replacing the slowest component with a faster counterpart).

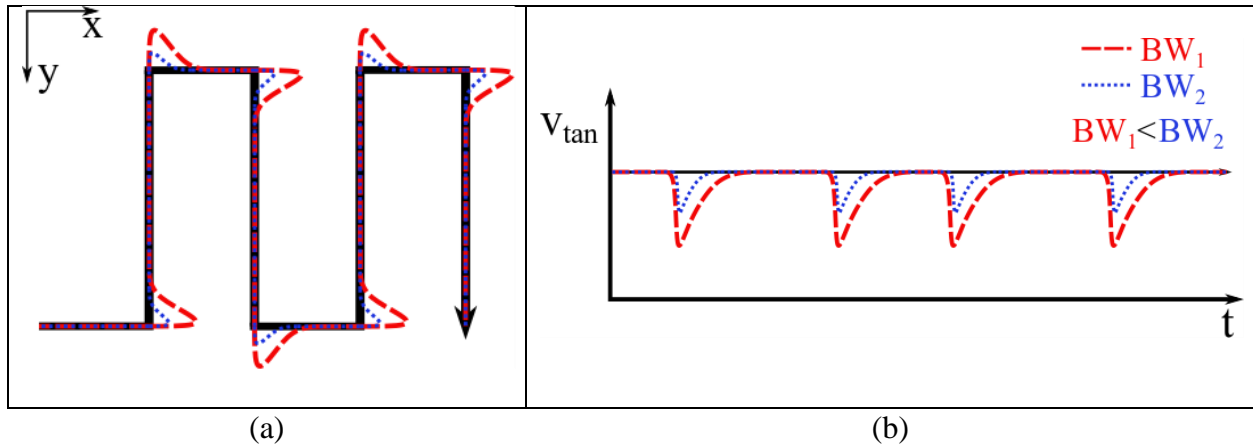


Figure 1.2: Example of two systems with different bandwidth responding to sudden changes in commanded position.

This thesis will focus on modelling the electron beam deflection system, such that an understanding of the systems dynamics is achieved. Once a model of the deflection system is developed and any system parameters are identified, alterations to the system that reduce beam trajectory errors will be discussed. These system changes will include hardware changes, and controller design. With a thorough understanding of the electron beam's dynamic position response, complex process control strategies can be explored more confidently.

Chapter 2: Literature Review

Metal AM is a heavily researched topic globally, due to the promising benefits in the aerospace and biomedical industries and the advancements required for the technology to become economically viable. As such there has been a steady influx of work studying the properties and production techniques of metal AM produced parts. This chapter presents a brief review of past research into the process control of EBM and its effects on part properties. Previous work on the control of electron beam deflection systems and other nonuniform magnetic field generators will also be reviewed, including a review of control techniques in scanning electron microscopes (SEM), and nuclear magnetic resonance imaging (NMRI) machines.

2.1 EBM Process Control

Parts produced from EBM are prone to various defects, which degrade the parts mechanical properties and geometric accuracy. A part that has been successfully produced with additive manufacturing should have part strengths comparable to their subtractive manufactured counterparts. Edwards et al. [7] studied the properties of EBM produced parts showing that part porosity is the dominate factor determining their mechanical strength. Tammas-Williams et al. [6] investigated the effect of EBM process parameters such as beam power and trajectory on the porosity of printed parts. Further, by measuring the part porosity for varying beam trajectories, the work demonstrates the impact that an inaccurate or low responsivity electron beam deflection system may have on the final part strength. Al-Bermani et al. [8] investigated the formation of microstructure within EBM produced parts and the consequent effect on the part's mechanical properties. Additionally, the work demonstrated that the build temperature had a significant effect

on the microstructure and properties of the finished part. This idea was applied to a commercial EBM machine by Narra et al. [2], by altering the process parameters within the EBM machine to provide location specific microstructure within an EBM produced part. Beyond part porosity and microstructure, the mechanical properties of a part may be dependent on dimensional accuracy, especially in cases where topological optimization is utilized, as shown by C.J. Smith et al [9]. This work also highlights the importance of heat management within truss structures in the reduction of dimensional inaccuracies. N. Béraud et al. [10] simulated the EBM process and demonstrated an improvement in dimensional accuracy via optimization of the beam trajectory. All of these works show the importance of process parameters such as the beam trajectory in ensuring the success of the EBM process, demonstrating the need for a broader EBM process window in the development of EBM AM.

2.2 Control of Electron Beam Deflection

To increase the accuracy of the beam trajectory during the EBM process and broaden the process window of EBM it is essential that the dynamic response of electron beam deflection system is characterized, and appropriate control techniques are employed. A mechanism that may dominate the dynamic response of beam deflection systems are eddy current losses within the electron beam gun structure. Eddy currents can induce lag in the beam position response, thereby reducing the deflection system's responsivity. Additionally, crosstalk between the axes of a beam deflection system may induce further errors in the beam's position on the build plate. Commercial EBM machines currently require a time-consuming calibration step prior to beginning the part production process, with the calibration results utilized for open-loop control of beam position. The electron beam position response in an electron beam welding machine was modelled by Oltean

and Abrudean, and Oltean and Dulău [11–13], with the beam trajectory through a nonuniform magnetic field modelled. These works demonstrate a linear relationship between the current within the deflection coils of the electron beam gun and the beam position. However, this work neglects the effect of eddy currents losses in the electron beam gun or crosstalk between the x- and y- axes of the deflection system. Thong and Breton, Thong and Li, and Lee and Thong [14–16] measured the dynamic response of a single axis of a beam deflection system within an SEM machine. These works investigate how the eddy current losses within the electron beam gun dominates the dynamic response of beam position, and employed open-loop control techniques, such as pole-zero cancellation and pre-filters, to increase the responsivity of the deflection system. Alternatively, Nisha et al. [17] demonstrated the utility of altering conductive paths of eddy currents in the electron beam gun to reduce the lag induced on the beam position response by the eddy currents. The eddy current reduction and compensation methodologies discussed for electron beam guns in SEM's may be applied to electron beam guns in EBM. However, the scan signals within SEM systems are less complex than the melt profiles in EBM, such that a complete model of the electron beam position within the system is not required.

Similar to the coils within an electron beam gun, the gradient magnetic field generating coils in NMRI machines require control systems to overcome the error induced by eddy currents and axes crosstalk. The patent US4585995 [18] describes a control system to suppress the effects of eddy currents on the gradient magnetic field within the NMRI chamber. The control system relies on measurement of the eddy current's time constants to provide the appropriate compensation signals to the gradient field generating coils. The patent US7050388B2 [19] describes an analog circuit that provides compensation signals to the gradient field producing coils in an NMRI machine to

compensate for the errors induced by crosstalk between the machine's axes. This invention is an open-loop control technique and relies on an accurate model of the crosstalk, otherwise over or under compensation will occur. Although these works do not work directly with EBM or electron beam guns, the control techniques they introduce may be implemented in EBM to reduce errors in beam trajectory during operation.

2.3 Summary

The presented works on EBM and the control of electron beam deflection systems provide a practice gap, which this thesis will begin the work of fulfilling. For EBM to become industrially viable as a manufacturing method, it is essential that defects within EBM produced parts are minimized to reduce the cost generated by failed prints. Further, the versatility of the EBM machines must be broadened, such that more topographically complex structures may be produced with adequate mechanical properties and low dimensional error. To accomplish these goals control techniques must be employed in the EBM machine's beam deflection system, with the goal of increasing the bandwidth of the beam position response. The presented literature shows some open-loop control techniques as well as hardware alterations, which begin to increase the responsivity of electron beam deflection systems. However, in some of the literature the errors induced by eddy currents are neglected, and in all the works pertaining to electron beam deflection systems the errors induced by crosstalk between the system's axes is neglected. The controllers employed in gradient field generators within NMRI provide insight into the prediction and compensation of errors induced by crosstalk between the system axes.

Chapter 3: Model of Electron Beam Gun

This thesis will provide a model of the electron beam gun, which is responsible for the generation and control of the heat source utilized in EBM. The electron beam gun is segmented into four parts as shown in Figure 3.1: 1) the electron gun, 2) astigmatism system, 3) focusing system, and 4) deflection system. Each part of the electron beam gun will be discussed separately in this chapter in the order in which they interact with the electron, and the information relevant to the modelling of the electron beam's position will be highlighted.

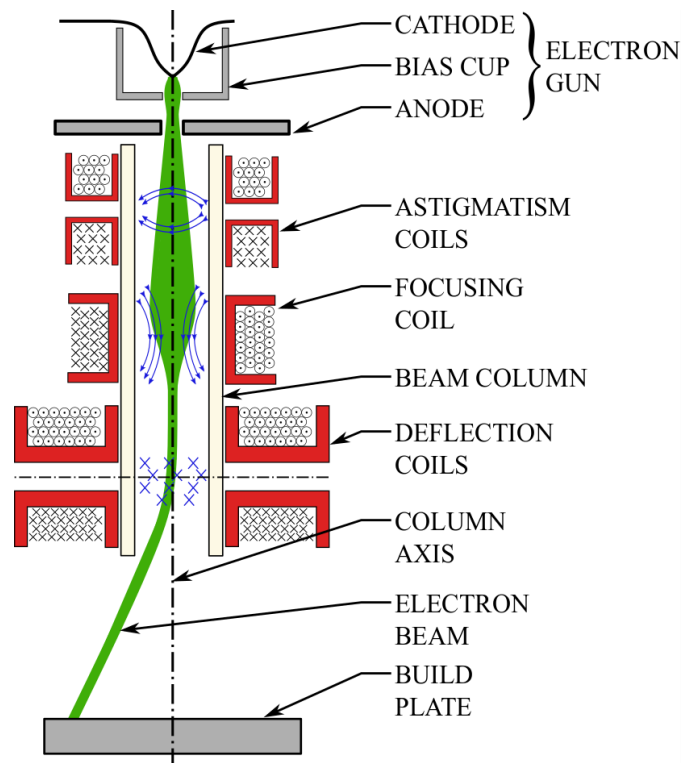


Figure 3.1: Diagram of electron beam gun components.

3.1 Electron Gun

The electron beam is generated by the electron gun, which is positioned above the build chamber.

The electron gun is comprised of three components: 1) the cathode or filament, 2) the bias cup,

and 3) the anode. The power of the beam, P_{beam} , measured in Watts, is determined by the electron gun. The beam power is evaluated from the potential difference between the cathode and the anode, called the accelerating voltage, and the current flow within the electron beam. Beam power can be expressed as:

$$P_{beam} = V_A I_{beam} \text{ [W]} \quad (3.1)$$

where, V_A [V] is the accelerating voltage and I_{beam} [A] is the current of the electron beam. The accelerating voltage is evaluated as the electric potential difference between the cathode and anode:

$$V_A = V_{an} - V_{cat} \text{ [V]} \quad (3.2)$$

where, V_{an} [V] is the voltage of the anode and V_{cat} [V] is the voltage of the cathode. The current of the electron beam is controlled by the bias cup. Figure 3.2 shows a diagram of electron beam generation, with a circuit diagram to represent the potential differences between the three components. This section will provide a more detailed explanation of each component and how it effects the beam's power.

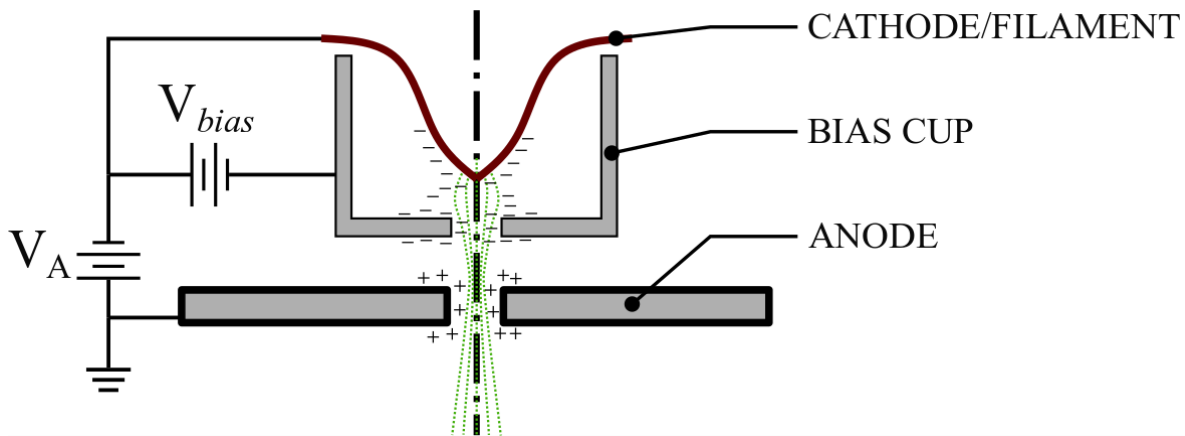


Figure 3.2: Diagram of electron beam gun with potential differences between the three components represented by a simple circuit diagram.

3.1.1 Cathode

The cathode or filament is the source of electrons for an electron beam gun. In high current electron guns, such as those used in EBM, commonly used cathodes are single crystal tungsten filaments or lanthanum hexaboride (LaB6) crystals. To generate an electron beam, the electrons within the cathode must be excited sufficiently such that they overcome the bonding energy of the cathode material. Electron excitation is achieved via a large electric potential (V_{cat}) applied to the cathode. The number of electrons emitted by the cathode based on the applied electric potential, V_{cat} , is determined by the cathode material's work function. The cathode's work function can be decreased by heating the cathode via an electrical current in the cathode or by a laser heat source, thereby increasing the number of electrons emitted by the cathode for all values of electric potential applied to the cathode. The emitted electrons have an electrical potential energy equal to the electric potential applied to the cathode. It is desirable to control the current of the electron beam without altering the potential energy of the emitted electrons. Therefore, rather than using the cathode work function to set the beam current, the current is controlled by the bias cup.

3.1.2 Bias Cup

The bias cup has a negative potential, which is more negative than the potential of the cathode. The bias cup generates a magnetic field that a virtual aperture on the cathode, reducing the number of electrons that leave the cathode surface, thus reducing the current of the beam (I_{beam}). By increasing the negative potential of the bias cup, the size of this virtual aperture can be reduced. This reduction would cause less electrons to leave the cathode surface, consequently reducing the beam's current [20].

Another feature of the bias cup is its stabilization of the beam current. If noise or a high voltage surge were to affect the voltage source of the cathode, the current of electrons emitted from the cathode would be affected according to the work function of the cathode material. However, if the bias cup potential rose an equal amount as the cathode potential, the additional emission current would be cancelled out by the decrease in the virtual aperture size. Therefore, if the difference of potentials between the cathode and the bias cup can be maintained, a less noisy and more stable beam current would be achieved.

To maintain the difference in potentials between the cathode and bias cup, the two components use the same high voltage source and the bias cup is supplied its additional negative potential by another voltage supply (V_{bias}), as shown in Figure 3.2. The bias supply can be a varied, such that the ratio of potentials between the cathode and bias cup can be altered. Therefore, by controlling the value of V_{bias} , the user may modulate the beam current in the EBM, without having to alter the potential of the cathode and consequently the emitted electrons.

3.1.3 Anode

The anode is a conductive aperture that is positioned below the cathode and bias cup and has a positive potential relative to the cathode. Typically, the anode is connected directly to ground, providing it with zero electric potential ($V_{an} = 0$ V), making the potential difference between the anode and cathode equal and opposite to the potential of the cathode ($V_A = -V_{cat}$). As mentioned above, the anode-cathode potential difference is called the accelerating voltage (V_A). After the electrons pass through the bias cup, they are attracted to the relatively positive potential of the anode. This attracting force causes the electrons to accelerate through the aperture in the anode.

The electron acceleration can be modelled as a transfer of electron energy from electric potential energy (PE_e) to kinetic energy (KE_e). The electric potential energy of the electrons emitted by the cathode is equal to the cathode's potential multiplied by the charge of the electron, and after passing through the anode, the electric potential energy of the electrons will be equal to the potential of the anode multiplied by the charge of the electron. The electric potential energy is transferred to kinetic energy as the electron is accelerated. Therefore, the kinetic energy of the accelerated electrons (KE_e) is equal to the difference of potentials of the cathode and anode, or the accelerating voltage (V_A), multiplied by the charge of the electrons expressed as:

$$\Delta PE_e = KE_e = qV_A \text{ [J]} \quad (3.3)$$

where, q is the charge of an electron ($q = 1.61 \times 10^{-19}$ C). The velocity of the accelerated electrons can be determined from their kinetic energy. Since the electrons are travelling at velocities greater than half the speed of light, relativistic corrections are applied to the particle's momentum using the Lorentz factor. The Lorentz factor can be expressed as a function of electron velocity:

$$\gamma(v_0) = \frac{1}{\sqrt{1 - \left(\frac{v_0}{c}\right)^2}} \quad (3.4)$$

where v_0 is the magnitude of the electron velocity, and c is the speed of light ($c = 3.00 \times 10^8$ m/s). The Lorentz factor is applied to the kinetic energy of the electrons as follows:

$$KE_e = \frac{\gamma m_e v_0^2}{2} \text{ [J]} \quad (3.5)$$

where, m_e is the rest mass of the electrons ($m_e = 9.11 \times 10^{-31}$ kg). By equating the change in potential energy (equation (3.3)) and kinetic energy (equation (3.5)) of the electrons, the velocity of the electrons can be described as a function of accelerating voltage:

$$v_0(V_A) = c \sqrt{1 - \frac{m_e^2 c^4}{(qV_A + m_e c^2)^2}} \quad [\text{m/s}] \quad (3.6)$$

By plotting the velocity for a range of accelerating voltages, it is possible to visualize the nonlinear effects induced by relativistic momentum. Figure 3.3 shows the relationship between accelerating voltage and electron beam velocity for accelerating voltages up to 200 kV, as well as the relationship between accelerating voltage and Lorentz factor, such that relativistic effects can be visualized.

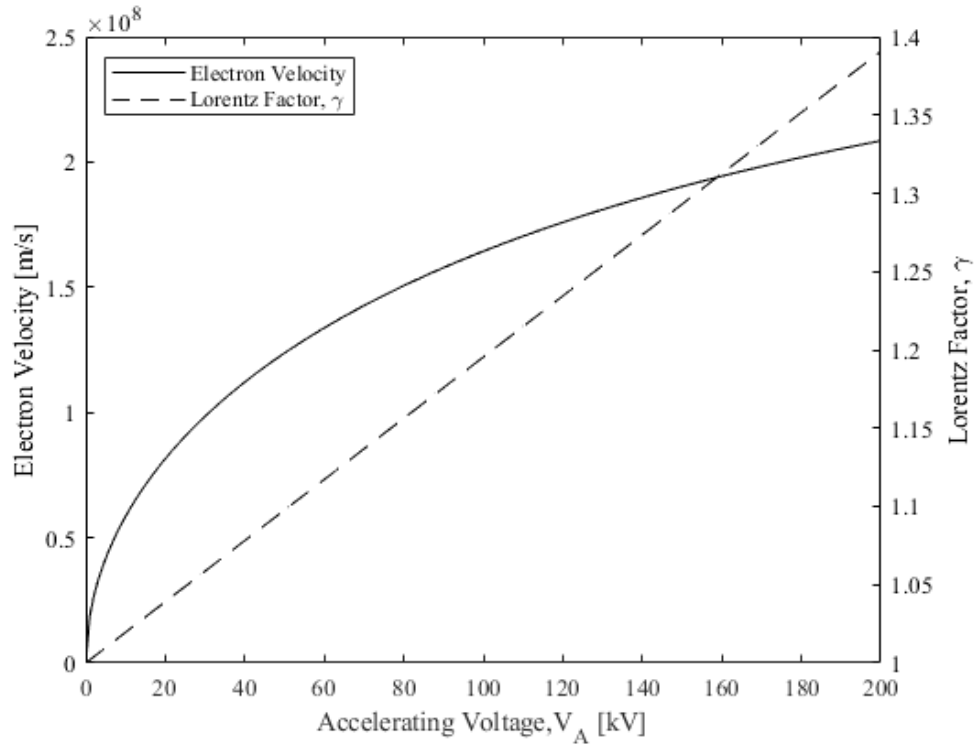


Figure 3.3: Effect of accelerating voltage on electron velocity and Lorentz factor.

After the anode, the beam is a diverging beam with a velocity coaxial to the electron beam gun center axis. Further beam manipulation will be conducted using electromagnetic coils, which induce no work on the electron beam. Therefore, the magnitude of electron velocity in each

electromagnetic subsystem can be assumed to be equal to the velocity generated by the accelerating voltage.

3.2 Astigmatism System

The electron beam produced by the electron gun contains artifacts that make it difficult or impossible to reduce the beam diameter to the small size desired for EBM applications. Namely, the electron beam has a non-circular cross-section and contains spherical aberrations. The astigmatism system's function is to correct the beams cross-section to a uniform circle and remove the aberrations. The circular beam cross-section is desired such that the energy input into the material may be more predictable and simpler to model. Removal of aberrations from the electron beam is necessary so that the beam diameter can be reduced for finer application of energy into the parts surface. The astigmatism system is a multi-pole electromagnetic system and may contain upwards of 24 poles. Previous works have investigated the modelling and control of astigmatism systems for cross-section correction and aberration removal in EBM and similar systems [21], [22].

3.3 Focusing System

After the electron beam passes through the anode, the beam is diverging from the column axis. The focusing coil is an electromagnetic coil wound around the beam column, which produces an axial-symmetric magnetic field that forces the previously diverging electron beam to converge on a desired focal point. The amount of current passing through the focusing coil determines the focusing power of the system, with greater current signals producing a shorter focal length. Therefore, the diameter of the electron beam on the build plate can be controlled by varying the

current within the focusing coil. The magnetic flux lines at the center of the focusing system are parallel to the to beam column axis. Since the force acting on a moving charge through a static magnetic field acts perpendicular to charge velocity and field direction, the focusing field only acts on electrons which are not travelling vertically. For the remainder of this thesis the output of the focusing system will be an electron beam that is assumed to be travelling coaxially with the beam column.

3.4 Deflection System

The beam position is controlled by an electromagnetic deflection system, consisting of two pairs of multi-layer air coils aligned perpendicular to each other, such that each pair controls the beam position along a separate axis. The coils in an axis are connected in series such that an equal amount of current passes through each coil. This is shown in the top view of a deflection coil system in Figure 3.4b. The coils are positioned outside a column which contains the ultra-high vacuum necessary to generate an electron beam. The electron beam is deflected through the force applied by the magnetic flux density, generated by the coils on the moving electrons. The magnetic flux density is generated by the coils via a current passing through the windings. A power amplifier supplies the current proportional to voltage commands sent from a computer. The voltage commands are generated based on the designed reference position profiles.

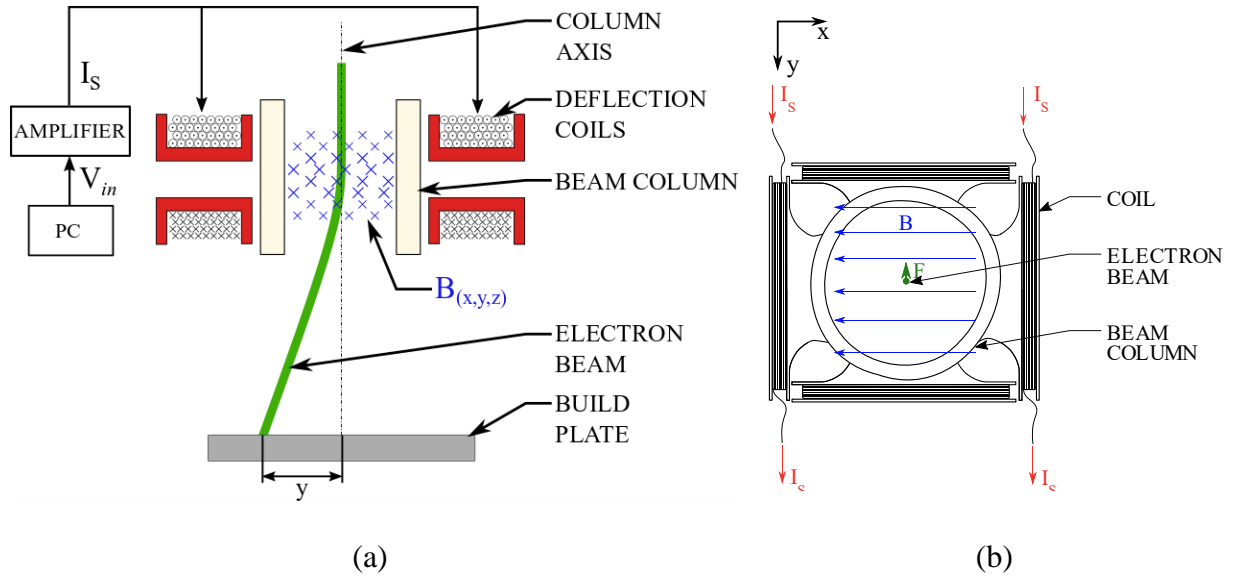


Figure 3.4: (a) Diagram of electron beam deflection system. (b) Top view of electron-beam deflection system.

The dynamics of the deflection system has been modelled in five stages as shown in the two-axis block diagram in Figure 3.5: 1) current amplifier, 2) deflection coil, 3) beam column, 4) beam deflection, and 5) crosstalk. The inputs of the deflection system are the voltage commands ($V_{in,x}$, $V_{in,y}$) sent by the EBM control computer, and the output of the system is the beam position (x , y) on the build plate.

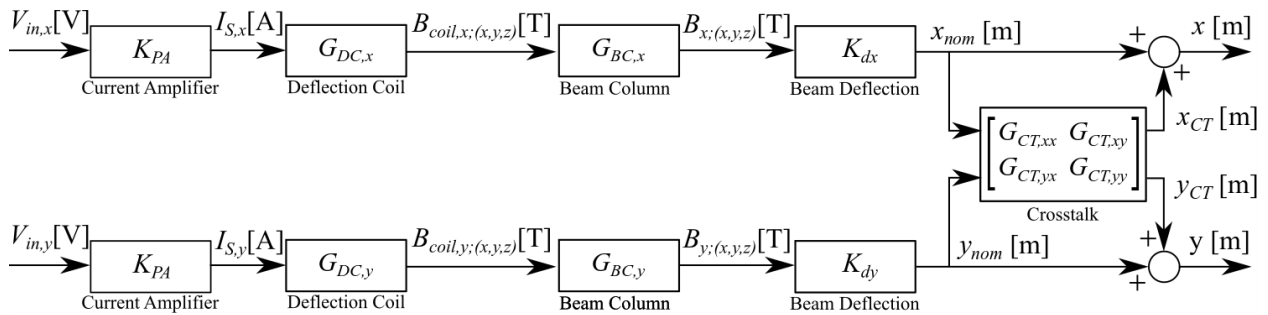


Figure 3.5: Block diagram of two-axis beam deflection system. Units: Current [A], magnetic flux density [T:

Tesla = 10^4 Gauss]

Each stage of the deflection system has been modelled independently with a transfer function provided for each stage. Beam positions x and y can be evaluated as a combination of the individual stages' transfer functions as:

$$\begin{aligned} \begin{Bmatrix} x(s) \\ y(s) \end{Bmatrix} &= K_{PA} \begin{bmatrix} G_{DC,x}(s)G_{BC,x}(s)K_{d,x} & 0 \\ 0 & G_{DC,y}(s)G_{BC,y}(s)K_{d,y} \end{bmatrix} \dots \\ &\begin{bmatrix} G_{CT,xx}(s) & G_{CT,xy}(s) \\ G_{CT,yx}(s) & G_{CT,yy}(s) \end{bmatrix} \begin{Bmatrix} V_{in,x}(s) \\ V_{in,y}(s) \end{Bmatrix} \text{ [m/s]} \end{aligned} \quad (3.7)$$

The following subsections of this chapter will describe the formulation of these transfer functions and the identification of the parameters within each transfer function.

3.4.1 Current Amplifier

The input into the current amplifier is the voltage command, V_{in} , sent from the EBM control computer, and the output is the current command, I_s . It is desirable that the current amplifier produces a current command linearly proportional to the input voltage. Therefore, the current amplifier should be selected such that it has high bandwidth relative to the rest of the deflection system (e.g. 50kHz), such that it may be modelled as a constant gain K_{PA} . The gain is identified from harmonic voltages supplied to the amplifier from DC to 1kHz and current output measurements.

$$\frac{I_s(s)}{V_{in}(s)} = K_{PA} \text{ [A/V]} \quad (3.8)$$

3.4.2 Deflection coil

The input to the multi-layer deflection coils is the current, I_S , supplied by the current amplifier. The output of the deflection coil is the generated magnetic flux density, B_{coil} [T], which interacts with the deflection system's beam column. The model of the deflection coil will be presented in two parts. First, the current behavior within the deflection coil will be modelled using equivalent circuits to determine which proportion of the input current will contribute the generation of magnetic flux density. Second, the generation of magnetic flux density based on the contributing current will be modelled to determine the output of deflection coil.

3.4.2.1 Deflection Coil Equivalent Circuit

The coils of the deflection system are multi-layer air coils of copper wire with a thin layer of Kapton insulation. The coils DC-resistance, inductance, and parasitic capacitance were modelled as a lumped parameter equivalent circuit, shown in Figure 3.6a. The DC-resistance and self-inductance is in series and the parasitic capacitance is modelled in parallel [23].

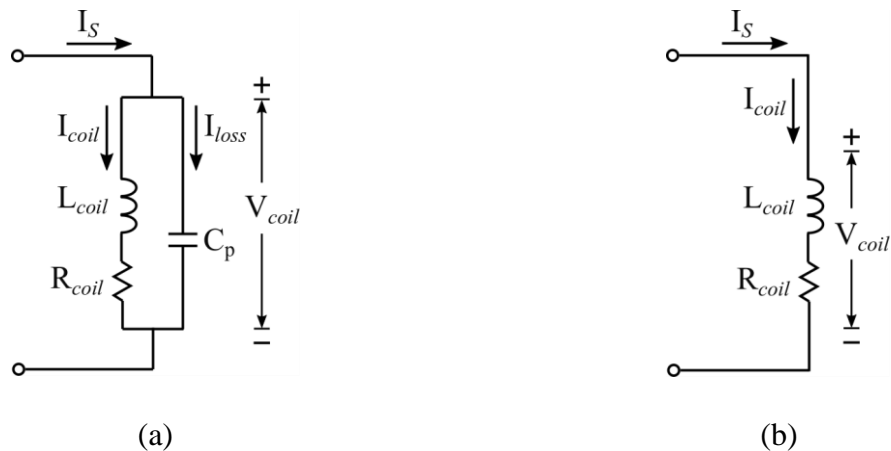


Figure 3.6: (a) Equivalent circuit of multi-layer air coil. (b) Alternative equivalent circuit of multi-layer air coil with parasitic capacitance neglected.

The current through the inductor, I_{coil} , will generate the magnetic flux density that deflects the beam, whereas the current through the capacitance, I_{loss} , will not produce a magnetic field. Therefore, the frequency response of the current through the inductor, I_{coil} , was modelled with respect to the current supplied to the coil, I_{in} , and is evaluated as:

$$\frac{I_{coil}(s)}{I_S(s)} = \frac{1}{L_{coil}C_p s^2 + R_{coil}C_p s + 1} = \frac{\omega_{n,DC}^2}{s^2 + 2\zeta_{DC}\omega_{n,DC}s + \omega_{n,DC}^2} \text{ [A/A]} \quad (3.9)$$

The response is second order with unity gain and a natural frequency equal to the self-resonant frequency, $\omega_{n,DC}$ [rad/s] of the coil. $\omega_{n,DC}$ is evaluated from the coil inductance and parasitic capacitance as:

$$\omega_{n,DC} = \sqrt{\frac{1}{L_{coil}C_p}} \text{ [rad/s]} \quad (3.10)$$

The open-loop bandwidth of the coils is defined by the self-resonant frequency, $\omega_{n,DC}$, of the coil. If the parasitic capacitance of the coils is very low such that the self-resonant frequency of the deflection coils is above the operating frequency of the deflection system, the equivalent circuit of the deflection coil may be simplified to the circuit seen in Figure 3.6b. The simplified circuit is a resistance and inductance series circuit. By neglecting the parasitic capacitance, the current input to the deflection coil is directly preserved in the inductor, such that the current behavior in the coils can be modelled as unity gain component within the bandwidth of the deflection system:

$$\frac{I_{coil}(s)}{I_S(s)} = 1 \text{ [A/A]} \quad (3.11)$$

The parameters of the equivalent circuit were determined experimentally as described in Chapter 5 of this thesis.

3.4.2.1.1 Skin Effect

For an alternating current passing through a conductor, the current density distribution within the conductor may vary depending on the frequency of the current. As the frequency of the signal in the conductor increases, the magnetomotive force (MMF) applied by the moving electrons on the adjacent electrons in the conductor increases. This increase in MMF causes the current density distribution to become non-uniform; the current density in the center of the conductor decreases, and the current density along the outer boundaries of the conductor increases, as shown in Figure 3.7. This frequency induced non-uniformity is known as the skin effect.

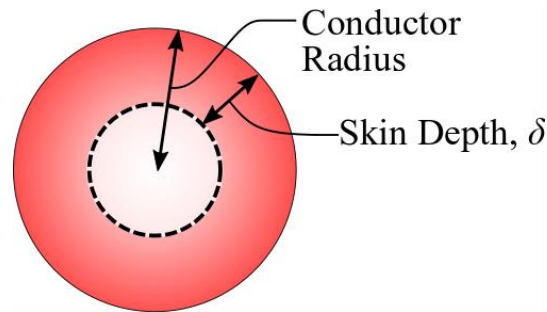


Figure 3.7: Skin effect in a circular conductor.

The outer region of the conductor where current density is increased is known as the skin, and the skin depth, δ , varies for different conductor materials and signal frequencies. The skin depth is expressed as:

$$\delta = \sqrt{\frac{\rho}{\pi f \mu_r \mu_0}} \text{ [m]} \quad (3.12)$$

where, ρ [Ω/m] is the resistivity of the conductor material, f [Hz] is the frequency of the current in the conductor, μ_r is the relative permeability of the conductor material, and μ_0 [$\text{m kg/s}^2\text{A}^2$] is the permeability free-space. If the skin depth is less than the radius of the circular conductor, the resistance of the conductor will increase as the effective area of current flow decreases. Therefore,

to avoid non-linear effects due to the skin effect, it is desirable that the radius of the conductor in the deflection coil is less than the skin depth for the maximum operating frequency of the deflection system. The skin depth in a copper conductor for frequencies up to 100 kHz is shown in Figure 3.8; from this plot it can be determined that the maximum radius for a conductor in a deflection system with a 5 kHz operating frequency is 0.922 mm.

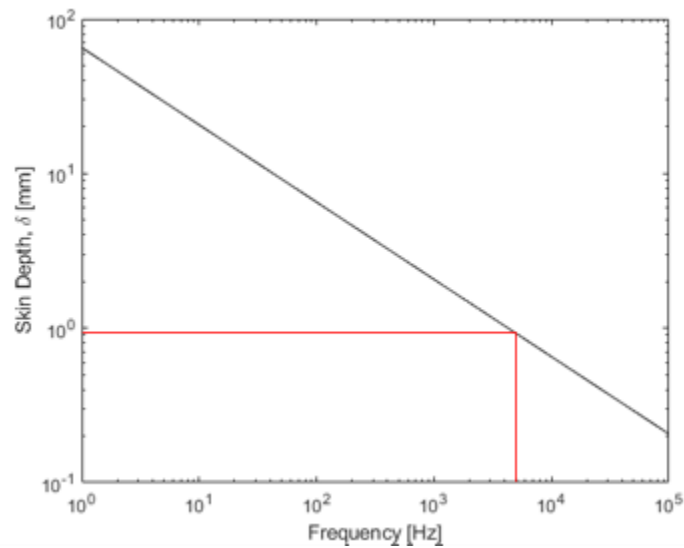


Figure 3.8: Signal frequency's effect on skin depth for a copper conductor.

For the remainder of this thesis the skin effect will be neglected, as the radius of the conductor in the deflection system is less than the 5 kHz skin depth.

3.4.2.1.2 Proximity Effect

Similar to the skin effect, the proximity effect causes the current density within a conductor to become non-uniform at high frequencies, increasing the conductor resistance. The proximity effect acts on bundled conductors such as the conductors in a multi-layer coil. As the current frequency of the bundled conductors increases, the current density will decrease near the center of the bundle and increase in the region of each conductor that is furthest from the center of the bundle, as shown

in Figure 3.9. The proximity effect is generally modelled in radio frequency systems at frequencies much greater than the bandwidth of the deflection system [23]. Therefore, the proximity effect will be neglected for the remainder of this thesis.

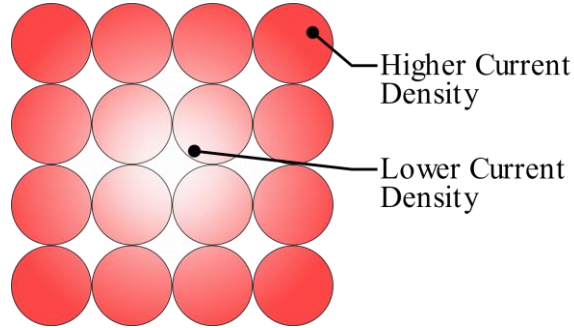


Figure 3.9: Proximity effect in conductor bundle.

3.4.2.2 Magnetic Flux Density Generation

The inductor current, I_{coil} , generates a magnetic flux density, B_{coil} , which is the output of the deflection coil stage, as shown in Figure 3.5. The generation of magnetic flux density due to current flowing through a conductor is described by Biot-Savart Law [24], which linearly relates current within a conductor to magnetic flux density at a point in space. To apply Biot-Savart Law, the multi-layer coil was simplified to a single conductor with the same cross section and a uniform current density. The magnetic flux density at a point outside the coils (x, y, z) was discretely computed over the entire cross-section and around the entire length of the windings. For a coil with a rectangular profile, as shown in Figure 3.10, discretization of the windings is segmented into linear and radial sections. The linear sections of the coil windings are meshed by discrete elements with a size of $(\Delta l, \Delta w, \Delta h)$, and the radial sections of the coil windings are meshed by discrete elements with a size of $(\Delta \theta, \Delta w, \Delta h)$. The magnetic flux density distribution is evaluated from Figure 3.10, with the linear sections being denoted as sections A, C, E, and G, and radial

sections being denoted B, D, F, and H. The magnetic flux density contribution of each section ($\mathbf{B}_{i;(x,y,z)}$ [T]) was evaluated by equation (3.13) for linear sections, and equation (3.14) for radial sections as follows:

$$\mathbf{B}_{i;(x,y,z)} \cong |\mathbf{I}_{coil}| \frac{\mu_0 N \Delta w \Delta h}{4\pi W H} \sum_{i=1}^{L/\Delta l} \sum_{j=1}^{W/\Delta w} \sum_{k=1}^{H/\Delta h} \frac{\Delta l (\hat{\mathbf{I}}_s \times \hat{\mathbf{a}}[(x,y,z);(l_i, w_j, h_k)])}{|\mathbf{a}[(x,y,z);(l_i, w_j, h_k)]|^2} \quad [\text{T}] \quad (3.13)$$

$$\mathbf{B}_{i;(x,y,z)} \cong |\mathbf{I}_{coil}| \frac{\mu_0 N \Delta w \Delta h}{4\pi W H} \sum_{i=1}^{\frac{\pi}{2}/\Delta\theta} \sum_{j=1}^{W/\Delta w} \sum_{k=1}^{H/\Delta h} \frac{R(k) \Delta\theta (\hat{\mathbf{I}}_s \times \hat{\mathbf{a}}[(x,y,z);(l_i, w_j, h_k)])}{|\mathbf{a}[(x,y,z);(l_i, w_j, h_k)]|^2} \quad [\text{T}] \quad (3.14)$$

where, μ_0 is the permeability of free space, $\hat{\mathbf{I}}_s$ is the unit vector of current flow direction, N is the number of turns, and $\hat{\mathbf{a}}[(x,y,z);(l_i, w_j, h_k)]$ is the unit displacement vector from discrete coil element to the point of interest (x,y,z) ($\hat{\mathbf{a}}$ is the unit vector of \mathbf{a}). The total magnetic flux density is evaluated from the sum of the contributions of the individual sections:

$$\mathbf{B}_{coil;(x,y,z)} \cong \sum \mathbf{B}_{i;(x,y,z)} \quad \text{for } i = A, B, \dots, H \quad [\text{T}] \quad (3.15)$$

The magnetic flux density from multiple deflection coils can be evaluated by applying equations (3.13), (3.14), and (3.15) to each coil and summing the resulting flux densities via superposition. The magnetic flux density ($\mathbf{B}_{coil;(x,y,z)}$) at each point (x,y,z) of the electron's path must be known to evaluate the force applied on each electron in the beam. Therefore, equations (3.13), (3.14), and (3.15) are used at every step of the beam deflection simulation. For simplification of the beam deflection evaluation, only the magnetic flux in the direction of the coil axis (shown B_{coilx} in Figure 3.10) will be considered, as the flux density in other directions is small enough to be neglected. Assuming the flux density generation is instantaneous with respect to the current in the

coil, the deflection coil's current to magnetic flux density response at any coordinate (x, y, z) is represented by a constant distributed gain $K_{B;(x,y,z)}$:

$$\frac{B_{coil;(x,y,z)}(s)}{I_{coil}(s)} = K_{B;(x,y,z)} \text{ [T/A]} \quad (3.16)$$

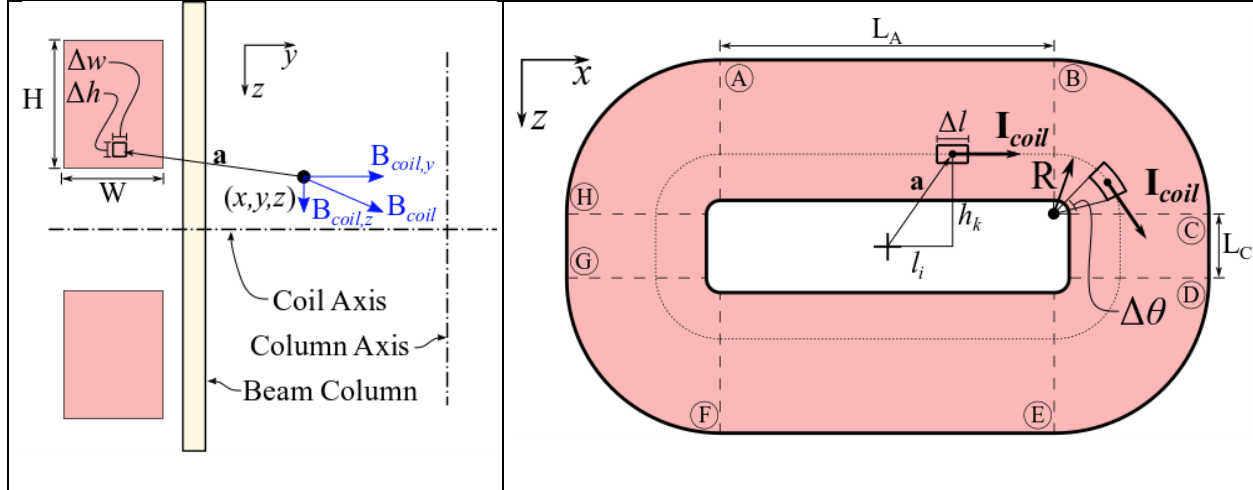


Figure 3.10: Side and front view of discretization of Biot-Savart Law for multi-layer air coil

Combining the transfer functions (3.9) and (3.16) provides the overall transfer function of the deflection coil, which evaluates the magnetic flux density distribution, $B_{coil;(x,y,z)}$, for a given current input, I_S , and can be expressed as:

$$\frac{B_{coil;(x,y,z)}(s)}{I_{in}(s)} = \frac{I_{coil}(s)}{I_{in}(s)} \cdot \frac{B_{coil;(x,y,z)}(s)}{I_{coil}(s)} = \frac{K_{B;(x,y,z)}}{L_{coil}C_p s^2 + R_{coil}C_p s + 1} \text{ [T/A]} \quad (3.17)$$

If the parasitic capacitance, C_p , is low enough such that the self-resonant frequency of the deflection coil is much greater than the deflection system bandwidth, the response of the deflection coil may be simplified to the following transfer function, which is the combination of transfer functions (3.11) and (3.16).

$$\frac{B_{coil;(x,y,z)}(s)}{I_{in}(s)} = K_{B;(x,y,z)} \text{ [T/A]} \quad (3.18)$$

3.4.3 Beam Column

The deflection coils are positioned around a hollow beam column, which contains the ultra-high vacuum necessary to generate an electron beam. If the column is constructed from a conductive material, a change in the magnetic field through the column will result in eddy currents within the column material. Eddy currents are electrical currents, which are generated on the surface of a conductive material in a changing magnetic field. As the rate of change in magnetic fields increases, the magnitude of eddy currents on a conductive surface within that magnetic field will also increase. These eddy currents will generate a magnetic field in the opposite direction of the rate of change of the magnetic field that is creating the eddy currents. Therefore, the eddy currents work against the changing magnetic field, resulting in any rapid change in the commanded magnetic field being delayed as the eddy currents resist the change in magnetic field [25], [26]. The magnetic field resulting from eddy currents are complex to analytically predict, therefore visualization of the effects of eddy currents have been analyzed through FEM simulation and experimentation. Since eddy currents act on the change in magnetic field, the effect of eddy currents will be visible in the frequency domain as an attenuation of high frequency signals. The eddy current induced lag within SEM deflection systems has been identified as a first order system [15] as:

$$\frac{B_{(x,y,z)}(s)}{B_{coil;(x,y,z)}(s)} = \frac{1}{\tau s + 1} \quad [\text{T}/\text{T}] \quad (3.19)$$

where $B_{(x,y,z)}(s)$ is the effective magnetic flux density experienced by the electrons in the beam, and τ is the time constant of the eddy current induced lag contributed by the beam column. The time constant, τ , is identified through FEM simulations and experimentation. The beam column transfer function can be simply converted to an FRF by replacing the replacing the Laplace operator with a frequency operator ($s = j\omega$).

$$\frac{B_{(x,y,z)}(j\omega)}{B_{coil;(x,y,z)}(j\omega)} = \frac{1}{j\omega\tau + 1} \quad [\text{T}/\text{T}] \quad (3.20)$$

The eddy current induced lag is the slowest stage of the electron beam deflection system, thereby dictating the bandwidth of the system. Therefore, understanding the dynamics of this stage and how the dynamics are determined is essential for increasing the bandwidth of the electron beam deflection system. This thesis will present the measured time constants of beam column stages and will discuss control strategies and changes to system hardware. Improvements in the beam column stage's responsivity will increase the responsivity of the electron beam deflection system.

3.4.4 Electron Deflection

With a known magnetic flux density distribution, $B_{(x,y,z)}$, it is possible to predict the trajectory of the electron through the deflection system and nominal beam position on the build plate (x_{nom} , y_{nom}). The position is referred to as nominal because as will be discussed in the following section, significant crosstalk error affects the beam's position, and this beam position prediction does not include that crosstalk position error. The focusing lens produces a converging beam traveling along

the z-axis of the system. The force vector, \mathbf{F} [N], on a moving charge through a magnetic field is described by the Lorentz force [27] as:

$$\mathbf{F}(x, y, z) = q[\mathbf{E}(x, y, z) + (\mathbf{v}(x, y, z) \times \mathbf{B}(x, y, z))] \text{ [N]} \quad (3.21)$$

where q [C] is the elementary charge, \mathbf{E} [V/m] is the electrostatic field vector, which is zero at every point in the deflection system, and \mathbf{v} [m/s] is the velocity vector of the electron (as shown in Figure 3.11). Due to the cross product seen in equation (3.21), the force on the electron acts perpendicular to both the electron velocity and the direction of the magnetic flux density. Therefore, to deflect the beam in the x-direction, the coils aligned on the y-axis must be supplied a current, generating a magnetic flux density perpendicular to the desired direction of deflection.

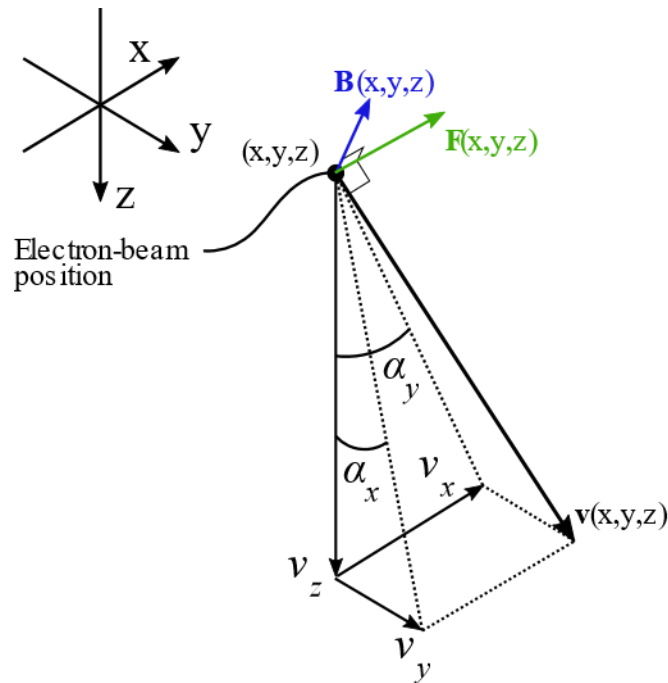


Figure 3.11 : Vector of electron beam velocity with angles of deflection shown.

The magnitude of the electron velocity is determined by the accelerating voltage parameter in the electron gun, as described in subsection 3.1.3 of this thesis. The deflection system does not perform any work on the electron, resulting in a constant magnitude of velocity throughout the system. The

direction of the velocity will change as the beam travels through the deflection system. However, the electron will always travel perpendicular to the magnetic flux density produced by the deflection coils, so the magnitude of the force only varies with the change in the magnetic flux density along the beam trajectory. The deflection induced by each axis of the deflection system will be evaluated individually, and the total deflection will be calculated via superposition of each axis. For simplification, when evaluating the deflection in the x-axis, only the magnetic flux density in the y-direction, B_y , generated by the coils aligned on the y-axis will be considered, and vice versa. With this simplification to the generated magnetic flux density, the Lorentz force in the x- and z- direction at any point (x, y, z) along the beam trajectory can be evaluated as:

$$F_x(x, y, z) = qB_y(x, y, z) \cdot v_z(x, y, z) \text{ [N]} \quad (3.22)$$

$$F_z(x, y, z) = qB_y(x, y, z) \cdot v_x(x, y, z) \text{ [N]}$$

The instantaneous acceleration can be evaluated from the Lorentz force and relativistic mass as:

$$\frac{d^2x}{dt^2} = \frac{1}{\gamma m_e} F_x(x, y, z) \text{ [m/s}^2\text{]} \quad (3.23)$$

$$\frac{d^2z}{dt^2} = \frac{1}{\gamma m_e} F_z(x, y, z) \text{ [m/s}^2\text{]}$$

The final velocity (v_x) and position (x_{nom}) of the beam are solved by evaluating equations (3.22) and (3.23) in the discrete time domain, with equations (3.13) , (3.14), and (3.15) used to compute the magnetic flux density ($B_y(x, y, z)$) at the electron's instantaneous position:

$$v_x(t + \Delta t) = v_x(t) + \frac{d^2 x_{nom}}{dt^2} \Delta t \text{ [m/s]} \quad (3.24)$$

$$v_z(t + \Delta t) = v_z(t) + \frac{d^2 z}{dt^2} \Delta t \text{ [m/s]}$$

$$x_{nom}(t + \Delta t) = x_{nom}(t) + v_x(t) \Delta t \text{ [m]} \quad (3.25)$$

$$z(t + \Delta t) = z(t) + v_z(t) \Delta t \text{ [m]}$$

The nominal deflection output on the build plate is evaluated as the position $x(t)$, when $z(t)$ is equal to the z -position of the build plate. The nominal deflection in the y -direction can be evaluated similarly using the magnetic flux density in the x -direction, B_x , generated by the coils aligned on the x -axis. For small deflection angles ($< 10^\circ$), the beam deflection stage may be modelled as a constant gain K_d , which is determined by a least squares fitting a linear relationship between static magnetic flux density distributions ($B_{y;(x,y,z)}(s)$, $B_{x;(x,y,z)}(s)$) and nominal beam deflection ($x_{nom}(s)$, $y_{nom}(s)$) as:

$$\frac{y_{nom}(s)}{B_{x;(x,y,z)}(s)} = K_{d,y} \text{ [m/T]}; \quad \frac{x_{nom}(s)}{B_{y;(x,y,z)}(s)} = K_{d,x} \text{ [m/T]} \quad (3.26)$$

The magnitude of the electron velocity, v_0 , affects the deflection gains, K_d , via two mechanisms. Firstly, from equation (3.21) it can be seen that as the velocity of the electrons increases, the Lorentz force that deflects the beam also increases, thereby increasing the output deflection and the deflection gain, K_d . Secondly, as the velocity of the electron beam increases the amount of time that the electrons spend in the effective field of the deflection system decreases, thereby decreasing the output deflection and the deflection gain, K_d . These two effects work against each other, thus it is complex to predict how altering the accelerating voltage, V_A , may alter the deflection gains of the system. Therefore, for any deflection system it is necessary to identify the accelerating voltage, V_A , to deflection gain, K_d , relationship with simulations or experiments.

3.4.5 Crosstalk

When the dynamic response of the two-axis deflection system was observed in experiments, a significant amount of crosstalk was observed between the axis of the system. That is, when a harmonic signal was sent to only one of the axes, deflection was observed in both axes. This crosstalk effect may be caused by a number of mechanisms: 1) mutual inductance between the coils in the axes, which is not captured by the current amplifier, 2) asymmetrical eddy currents within the beam column, 3) radio-frequency noise in the deflection coils inducing surface currents in the other axes, or 4) other magnetic harmonic effects. In this thesis an empirical crosstalk transfer function was fitted to the measured crosstalk, such that for any nominal beam position on the build plate (x_{nom}, y_{nom}) , the error in the beam's position on the build plate induced by crosstalk (x_{ct}, y_{ct}) can be predicted in real-time. The measured empirical model may be expressed as:

$$\begin{Bmatrix} x_{CT}(s) \\ y_{CT}(s) \end{Bmatrix} = \begin{bmatrix} \frac{\alpha_{CT} s}{\tau_{CT} s + 1} & -\frac{\alpha_{CT} s}{\tau_{CT} s + 1} \\ \frac{\alpha_{CT} s}{\tau_{CT} s + 1} & -\frac{\alpha_{CT} s}{\tau_{CT} s + 1} \end{bmatrix} \begin{Bmatrix} x_{nom}(s) \\ y_{nom}(s) \end{Bmatrix} \quad [\text{m}] \quad (3.27)$$

where, α_{CT} and τ_{CT} are the crosstalk parameters that must be identified from two-axis deflection experiments. The actual beam's position on the build plate can be predicted as the sum of the nominal beam position and the crosstalk position error:

$$x(s) = x_{nom}(s) + x_{CT}(s) \quad [\text{m}] \quad (3.28)$$

$$y(s) = y_{nom}(s) + y_{CT}(s) \quad [\text{m}] \quad (3.29)$$

This relationship can be simplified to the transfer function matrix from nominal position (x_{nom}, y_{nom}) , to actual position (x, y) as:

$$\begin{Bmatrix} x(s) \\ y(s) \end{Bmatrix} = \begin{bmatrix} 1 + \frac{\alpha_{CTS}}{\tau_{CTS} + 1} & -\frac{\alpha_{CTS}}{\tau_{CTS} + 1} \\ \frac{\alpha_{CTS}}{\tau_{CTS} + 1} & 1 - \frac{\alpha_{CTS}}{\tau_{CTS} + 1} \end{bmatrix} \begin{Bmatrix} x_{nom}(s) \\ y_{nom}(s) \end{Bmatrix} \text{ [m]} \quad (3.30)$$

Crosstalk between axes is a source of trajectory errors in the electron beam deflection system, as they behave similarly to a linear disturbance signal on the beams position. Therefore, understanding the crosstalk behavior in the deflection system is necessary, so that it may be removed with controllers that compensate for the crosstalk in real-time. Section 4.2 of this thesis discusses a feed forward crosstalk compensation controller aimed to reduce errors induced via axes crosstalk. Additionally, if the source of the crosstalk error could be identified and physically modelled, hardware alterations, which reduce the crosstalk may be possible. For example, if the crosstalk is identified to be caused asymmetrical eddy currents within the beam column, the crosstalk may be removed by replacing the conductive beam column with a nonconductive material, such as alumina (Al_2O_3).

3.5 Summary

The electron gun generates the electron beam, with the accelerating voltage and bias cup determining the magnitude of the electron beam velocity, v_0 , and beam current, I_{beam} , respectively. With equation (3.21) it can be seen that the electron beam velocity is proportional the magnitude of the deflection force on the electron beam. Further, the faster a beam is travelling the less time it will spend in the deflection system. Therefore, the accelerating voltage is an important parameter in the evaluation of beam deflection. Equation (3.6) shows how the magnitude of the electron beam velocity is determined from the accelerating voltage.

The electron beam deflection system has been segmented into five stages, with each stage's dynamic response being modelled and represented by a transfer function. The overall open-loop transfer function for a single axis of the beam deflection system, from input voltage to the current amplifier ($V_{in,x}, V_{in,y}$) to nominal output deflection ($x_{nom}(s), y_{nom}(s)$) can be expressed as:

$$\frac{x_{nom}(s)}{V_{in,x}(s)} = \left(\frac{I_{S,x}(s)}{V_{in,x}(s)} \right) \left(\frac{B_{coil;(x,y,z)}(s)}{I_{S,x}(s)} \right) \left(\frac{B_{(x,y,z)}(s)}{B_{coil;(x,y,z)}(s)} \right) \left(\frac{x_{nom}(s)}{B_{(x,y,z)}(s)} \right) \quad [\text{m/V}] \quad (3.31)$$

$$\frac{x_{nom}(s)}{V_{in,x}(s)} = \frac{K_{PA}K_BK_{d,x}}{(L_{coil}C_p s^2 + R_{coil}C_p s + 1)(\tau s + 1)} \quad [\text{m/V}]$$

$$\frac{y_{nom}(s)}{V_{in,y}(s)} = \left(\frac{I_{S,y}(s)}{V_{in,y}(s)} \right) \left(\frac{B_{coil;(x,y,z)}(s)}{I_{S,y}(s)} \right) \left(\frac{B_{(x,y,z)}(s)}{B_{coil;(x,y,z)}(s)} \right) \left(\frac{y_{nom}(s)}{B_{(x,y,z)}(s)} \right) \quad [\text{m/V}] \quad (3.32)$$

$$\frac{y_{nom}(s)}{V_{in,y}(s)} = \frac{K_{PA}K_BK_{d,y}}{(L_{coil}C_p s^2 + R_{coil}C_p s + 1)(\tau s + 1)} \quad [\text{m/V}]$$

Where $K_{d,x}$ and $K_{d,y}$ are dependent on the electron beam velocity, and consequently the accelerating voltage, V_A . If the self-resonant frequency ($\omega_{n,DC}$) of the deflection coil is much greater than the deflection system bandwidth, the response of the single-axis response may be simplified to:

$$\frac{x_{nom}(s)}{V_{in,x}(s)} = \frac{K_{PA}K_BK_{d,x}}{(\tau s + 1)} \quad [\text{m/V}] \quad (3.33)$$

$$\frac{y_{nom}(s)}{V_{in,y}(s)} = \frac{K_{PA}K_BK_{d,y}}{(\tau s + 1)} \quad [\text{m/V}] \quad (3.34)$$

The two-axis response of the system must include the crosstalk between the system's axes. By including the crosstalk, the beam's position ($x(s), y(s)$) is expressed as a function of the input voltages ($V_{in,x}, V_{in,y}$) as:

$$\begin{Bmatrix} x(s) \\ y(s) \end{Bmatrix} = K_{PA} \begin{bmatrix} 1 + \frac{\alpha_{CT} s}{\tau_{CT} s + 1} & -\frac{\alpha_{CT} s}{\tau_{CT} s + 1} \\ \frac{\alpha_{CT} s}{\tau_{CT} s + 1} & 1 - \frac{\alpha_{CT} s}{\tau_{CT} s + 1} \end{bmatrix} \dots \quad (3.35)$$

$$\begin{bmatrix} \frac{K_B K_{d,x}}{(L_{coil} C_p s^2 + R_{coil} C_p s + 1)(\tau s + 1)} & 0 \\ 0 & \frac{K_B K_{d,y}}{(L_{coil} C_p s^2 + R_{coil} C_p s + 1)(\tau s + 1)} \end{bmatrix} \begin{Bmatrix} V_{in,x}(s) \\ V_{in,y}(s) \end{Bmatrix} \text{ [m]}$$

The prediction of the K_B , $K_{d,x}$, and $K_{d,y}$ have been described in the above sections, with the validation of those predictions conducted through FEM simulation and experimentation. Each parameter in the deflection system transfer functions must be identified through experimentation and FEM simulation. The eddy current induced lag in the beam column stage and the crosstalk between axes are sources for trajectory errors in the electron beam. These trajectory errors may cause errors in the part to occur during the EBM process, so they should be minimized. Further, the eddy current induced lag limits the bandwidth of the deflection system, which directly limits the velocity of the beam on the build plate. Therefore, hardware alterations and control systems that reduce the eddy current induced lag should be implemented, thereby broadening the EBM process window.

Chapter 4: Position Control of Electron Beam

As discussed in section 3.4 of this thesis, there are two sources of linear error in the electron beam deflection system: 1) lag induced from eddy currents in the beam column, and 2) crosstalk between system axes. The eddy current induced lag can be reduced or removed by swapping the conductive beam column for a nonconductive beam column, such as a ceramic beam column. Alternatively, control systems can be designed that compensate for the eddy current induced lag in real-time. Without instrumentation to measure the magnetic flux density within the beam column, $B_{(x,y,z)}$, or the position of the electron beam on the build plate (x, y) , open-loop control strategies that predict the eddy current lag and crosstalk errors and send an appropriate compensating signal must be employed. This chapter presents both open-loop control strategies, beginning with open-loop compensation of eddy currents ending with a feedforward controller for crosstalk compensation.

4.1 Open-Loop Eddy Current Compensation

As discussed in Section 3.4.3 of this thesis, eddy currents within the beam column of the deflection system can decrease the system's bandwidth. The eddy current induced lag creates a first order response in the deflection system as shown in the transfer function (3.19), with a pole located at $p_{eddy} = 1/\tau$ rad/s. One option for decreasing the eddy current induced lag is implementing an open-loop controller, which predicts the lag and compensates for it with by amplifying the input signal, V_{in} , accordingly. The open-loop controller designed for this thesis has a pole-zero cancelation configuration, and would be placed in the system between the EBM control computer and the current amplifier as shown in the single-axis block diagram seen in Figure 4.1. The input

of the pole cancellation controller would be the input voltage, V_{in} , and the output would be a compensated voltage signal, V_c .

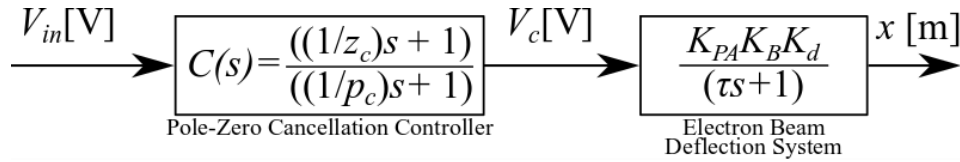


Figure 4.1: Block diagram of a single-axis deflection system with pole cancellation controller.

The pole in the open-loop response of the deflection system can be cancelled out with a zero, z_c , at the same location ($z_c = 1/\tau$ rad/s). However, placing a zero at a low frequency will cause all frequencies after the zero to be amplified. This amplification is undesirable as it will amplify high frequency noise and it will potentially saturate the amplifier for high frequency signals. To avoid either of these undesirable effects, a pole, p_c , should be placed in the controller's response at a frequency greater than the p_{eddy} . The resulting controllers transfer function (4.1) is a first-order system, and an example of the controller's open-loop bode plot is shown in Figure 4.2.

$$C(s) = \frac{\left(\left(\frac{1}{z_c}\right)s + 1\right)}{\left(\left(\frac{1}{p_c}\right)s + 1\right)} = \frac{(\tau s + 1)}{\left(\left(\frac{1}{p_c}\right)s + 1\right)} \quad (4.1)$$

The parameter values used on the experimental setup are $\tau = 1.73$ ms and $1/p_c = 0.3125$ ms.

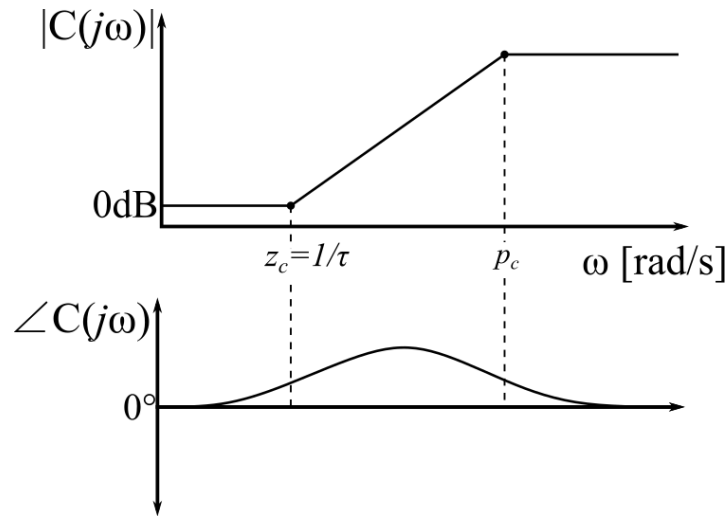


Figure 4.2: Example bode plot for designed pole-zero cancellation controller

The added pole, p_c , will create a new first-order response in the open-loop response of the deflection system, with a bandwidth equal to the position of the new pole. Therefore, to increase the responsivity of the deflection system as much as possible, p_c should be placed at as high a frequency as possible, while still avoiding amplifier saturation for normal deflection system operations. If the user wants to increase the bandwidth further, a more powerful current amplifier should be installed so that the saturation limit of the amplifier is increased, and consequently the pole, p_c may be placed at a higher frequency.

The effectiveness of pole-zero controllers is highly dependent on the accuracy of the zero placement. If the zero, z_c , is placed at a lower frequency than the eddy current induced pole, p_{eddy} , the zero may create more errors in the deflection system as it will be amplifying input signals beyond their desired values. If the zero, z_c , is placed at a greater frequency than the eddy current induced pole, p_{eddy} , the controller will not compensate entirely for the eddy current induced error.

4.2 Feed forward Crosstalk Compensation

As discussed in section 3.4.5 of this thesis, the two-axis deflection system output contains crosstalk error in the beam's position on the build plate. This error may be compensated for in real-time via a feed forward controller. A feed forward controller uses the input signal into a system and an accurate model of disturbance signals to predict the errors that may occur in the system output. The prediction of output error can then be inverted and added to the original input signal to correct for the error. For the electron beam deflection system, the error induced by crosstalk can be predicted from empirical model (equation (3.27)). The feed forward compensation controller will measure the input voltage, V_{in} , and will output a compensation voltage, V_c , in real-time based on the prediction of crosstalk current, x_{CT} . A two-axis block diagram of the electron beam deflection system with feed forward compensation included can be seen in Figure 4.3.

$$V_{c,x}(s) = \left(1 - \frac{\alpha_{CT} s}{\tau_{CT} s + 1}\right) V_{in,x}(s) + \left(\frac{\alpha_{CT} s}{\tau_{CT} s + 1}\right) V_{in,y} \quad [V] \quad (4.2)$$

$$V_{c,y}(s) = \left(\frac{-\alpha_{CT} s}{\tau_{CT} s + 1}\right) V_{in,x}(s) + \left(1 + \frac{\alpha_{CT} s}{\tau_{CT} s + 1}\right) V_{in,y} \quad [V] \quad (4.3)$$

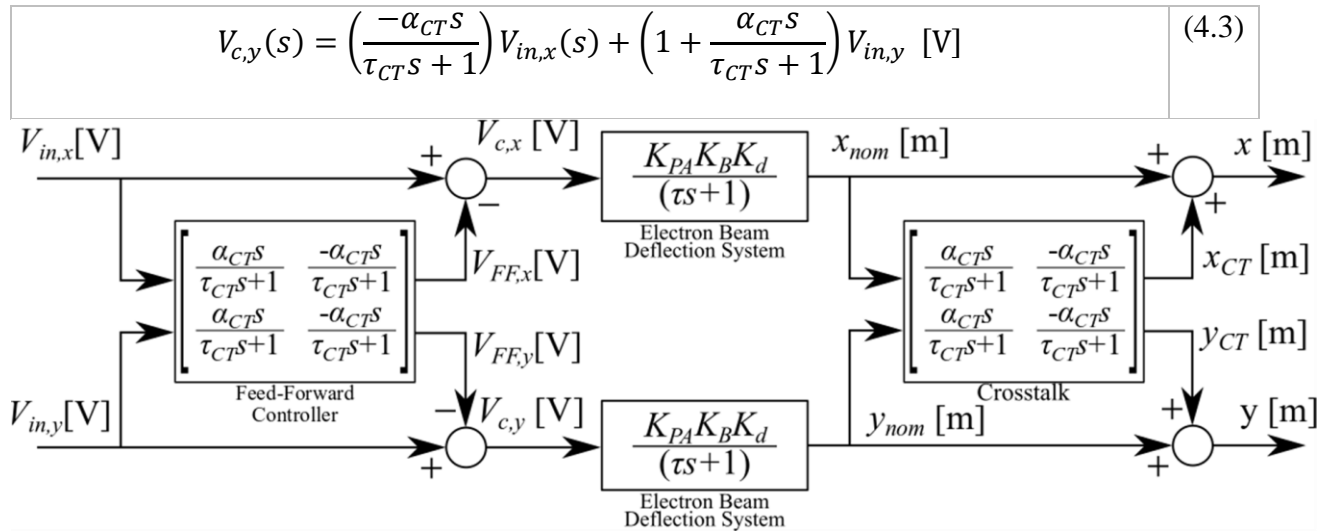


Figure 4.3: Block diagram of two-axis deflection system with feed forward crosstalk compensation.

Since the feed forward controller is an open-loop control technique, it relies heavily on the accuracy of the predictive model to effectively compensate for errors. If the predictive crosstalk

model does not match the actual crosstalk closely, the controller may under-compensate for crosstalk leaving some beam trajectory errors in the system. Alternatively, the predictive crosstalk model may over-compensate for actual crosstalk, which could cause greater errors in beam trajectory than the uncompensated system. Therefore, it is important for the parameters in the feed forward controller to be identified accurately via experimentation. Another detriment of the feed forward control technique is a lack of robustness. If the system's parameters shift with temperature or aging, the accuracy of the predictive model would be compromised. Therefore, calibration tests should be conducted regularly to refit the controller's parameters

Chapter 5: Simulation and Experimental Validation

The presented model was validated with FEM simulations, and experimental testing. First, the self-inductance, DC-resistance, and parasitic capacitance were measured experimentally to identify the deflection coil's resonance frequency. Then the distribution of flux density in the system was simulated and experimentally measured along the z-axis to validate the flux distribution prediction model presented in section 3.4.2.2. The response of the beam column was simulated and measured in the frequency domain to identify the time constant of the eddy current induced lag. An open-loop pole zero cancellation controller effectiveness for increasing the system's bandwidth was tested. The deflection of the electron beam in a static magnetic field was simulated and measured to validate the predicted deflection coefficient. Finally, the crosstalk error was measured in the frequency domain to identify parameters within the empirical crosstalk model. The feed forward controller for crosstalk compensation was tested, and the contouring error was measured and compared to the open-loop response.

5.1 Simulation and Experimental Setups

The model was validated on both single-axis and two-axis deflection systems. The two-axis deflection system is a Canmora EBM machine, which has an aluminum 6061 beam column. The exact geometry and winding configurations of the Canmora EBM deflection coils is unknown to the researchers. Therefore, the Canmora EBM machine was inadequate to validate the deflection coil equivalent circuit (section 3.4.2.1) and magnetic flux density generation model (section 3.4.2.2). To validate these models, a single-axis deflection test setup was designed and built, using deflection coils with known geometry and winding configurations, which were supplied by

Canmora. The single-axis test setup was also simulated in a FEM software to provide further validation of the deflection system model. This section of the thesis will describe the details of the single-axis test setup, as well as Canmora two-axis deflection system.

5.1.1 Single-Axis Test Setup

5.1.1.1 FEM Simulation Setup

All FEM simulations were completed with COMSOL Multiphysics software. A simplified model of the deflection system was generated, with coil geometry analyses, stationary studies, and frequency domain studies conducted on the model. The deflection coils were modelled as homogeneous multi-turn coils, with a uniform current density across the cross-section of the coils. The coil geometry and material were modelled to match the deflection coils seen in versions of the Canmora EBM machine. The coils were arranged in a configuration matching the Canmora EBM machine, and external single-axis deflection setup used in this work. The beam column diameter and thickness were modelled to match the beam column seen in Canmora EBM machines. However, as a simplification to the column geometry the top and base of the simulated column ended 100 mm from the axis of the coils. The beam column was modelled as a conductive domain and the material was varied to observe the effects of column conductivity on the frequency response of the deflection system. Figure 5.1 shows the FEM model geometry. To ensure convergence in the frequency domain simulations, vacuum space in the model was provided a conductivity of 1 S/m, which is low enough to avoid significant inaccuracy in the simulation results [28].

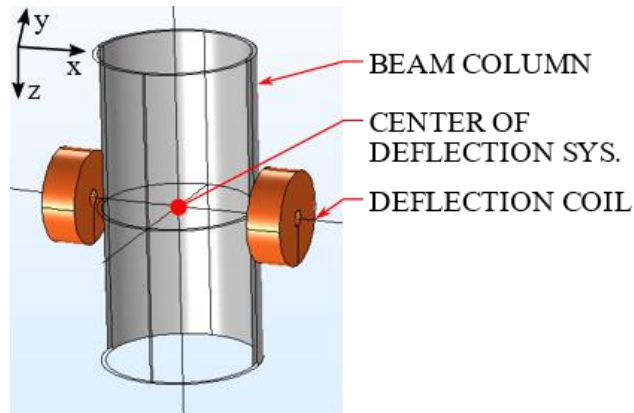


Figure 5.1: FEM model of beam deflection system.

The simulated stationary magnetic flux density solutions can be utilized as an input into COMSOL's particle tracing toolbox, to simulate the trajectory of an electron through the deflection system. The particles entering the simulated deflection system were provided a momentum based on the selected accelerating voltage, V_A , and evaluated from (3.6). The initial position of the particles was set to 250mm above the deflection coil axis, and co-axial to the beam column.

5.1.1.2 Single-Axis Test Setup

A single-axis deflection system was designed and built external to the EBM machine. The single-axis test setup's deflection coils and beam column were designed and supplied by Canmora. Therefore, the beam columns have the exact geometry seen in the Canmora EBM machines, and the deflection coils match those that will be installed in future Canmora EBM machines. The beam column could be swapped between experiments, such that different material beam columns could be tested. A single-axis gauss probe (F.W. Bell: STF71-0404-15 STD) was positioned on the center axis of the beam column and was connected to a gauss meter (F.W. Bell: Model 7010), which converted the magnetic flux density experienced by the probe into an analog voltage signal. The gauss probe is capable of measuring DC and AC signals. The DC measurement mode has a

frequency range of DC to 100 Hz, the AC measurement mode has a frequency range of 20 Hz to 20 kHz. The specified accuracy of the gauss probe and meter is 2% of the measurement range, which was maintained at ± 3 mT for all experiments. The Gauss meter produced a nonlinear lag in the magnetic flux density signal, induced by built-in filters and computational propagation lag, so the phase delay measured via the meter became difficult to interpret and is not declared in this work. The fixture that held the gauss probe was mounted to a hollow shaft potentiometer, such that the angle of the gauss probe's measurement direction could be measured. The deflection coils and beam column were placed on legs with adjustable height, consisting of ABS plastic, and Delrin polycarbonate. The single-axis test setup's leg material was chosen such that it did not interact with the magnetic field produced by the deflection coils. The adjustable height of the coil platforms allows the position of the gauss probe along the z-axis to be varied along discrete steps of 10mm over a stroke of 160mm. A diagram and photograph of the external single-axis deflection system can be seen in Figure 5.2.

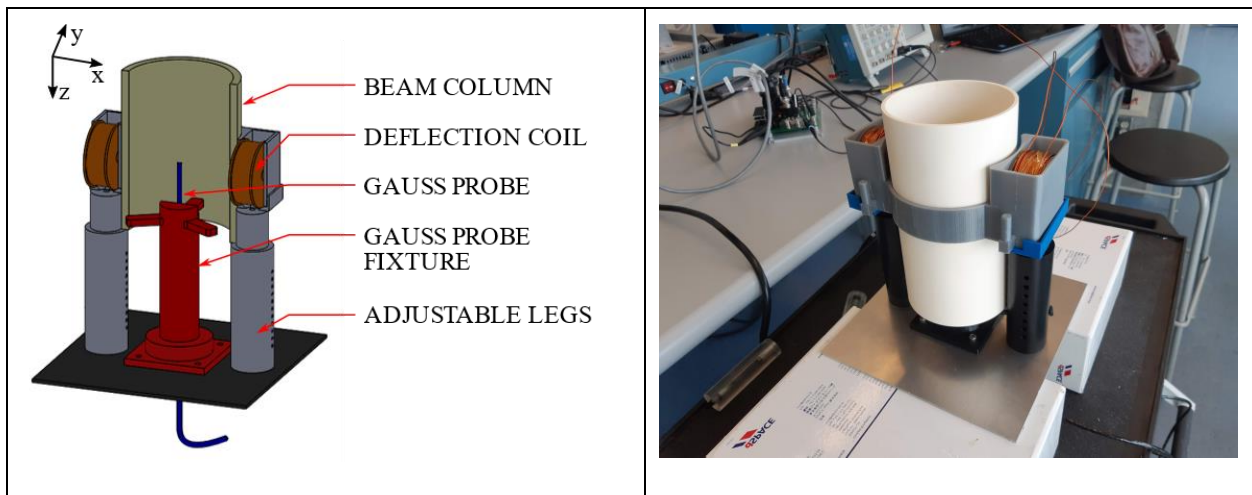


Figure 5.2: Diagram and photograph of external single-axis deflection system.

The current into the single-axis setup's deflection coils was supplied by a current amplifier, with adjustable bandwidth and gain. A circuit diagram of the current amplifier can be seen in Figure

5.3. The current amplifier consisted of a PA13 power amplifier in a non-inverting configuration providing a voltage gain, and OP27 operational amplifier for current control. The gain of the power amplification was adjusted via the resistors within its feedback loop. For all experiments the gain of the voltage stage was maintained at 11 V/V. The current control loop was configured as a proportional controller, with a DC gain of 0.89 A/V. The linear amplifier had a bandwidth of 20 kHz, which is four times the highest tested frequency of 5 kHz. Therefore, the linear amplifier was treated as a constant gain component with DC gain 0.89 A/V. The linear amplifier includes a current sensing resistor with a resistance of $R_S = 0.2 \Omega$. During experiments the voltage drop across the resistor was measured, and the current supplied to the deflection coils can be evaluated as:

$$I_S = \frac{V_S}{R_S} = 5V_S \text{ [A]} \quad (5.1)$$

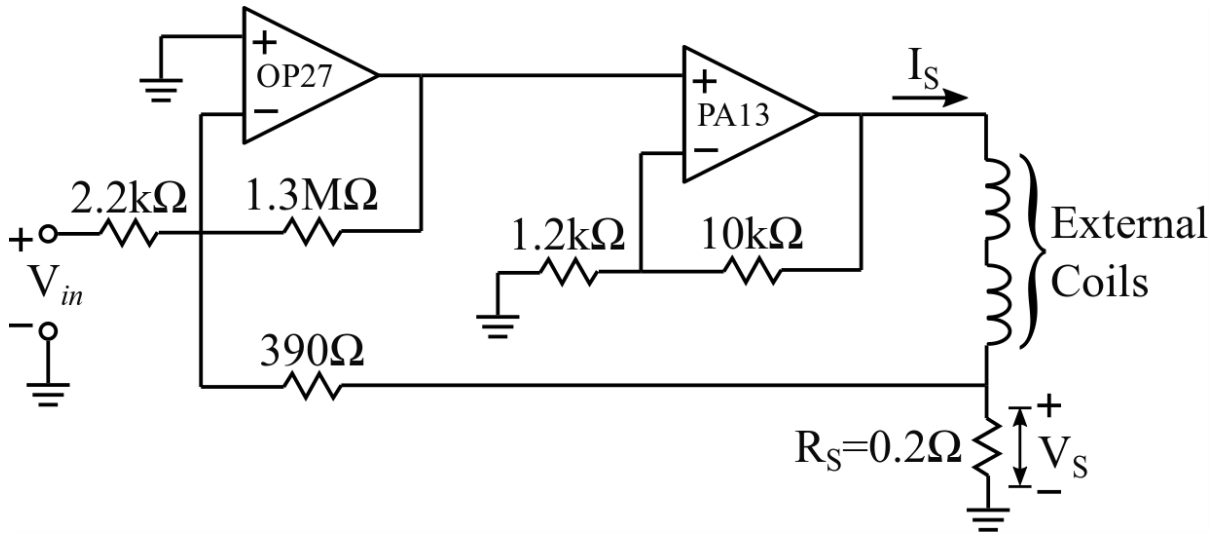


Figure 5.3: Linear amplifier used to provide current to external deflection coils.

Identification of the coils' DC-resistance, and self-inductance can be accomplished experimentally via a frequency sweep test of the coil impedance. When evaluating the DC-resistance, and self-

inductance of the external coils, it is necessary to account for the impedance added by the current sensing resistance. The FRF of the deflection coil impedance in series with the current sensing resistor, R_S , can be expressed as:

$$\frac{I_S(j\omega)}{V_{coil}(j\omega)} = \frac{-\omega^2 L_{coil} C_p + j\omega(R_{coil} + R_S)C_p + 1}{j\omega L_{coil} + R_{coil} + R_S} \quad [\text{A/V}] \quad (5.2)$$

where ω [rad/s] is the signal frequency. The magnitude and phase delay of the response of the coil can be expressed as:

$$\left| \frac{I_S(j\omega)}{V_{coil}(j\omega)} \right| = \frac{\sqrt{(\omega(R_{coil} + R_S)C_p)^2 + (1 - \omega^2 L_{coil} C_p)^2}}{\sqrt{(\omega L_{coil})^2 + (R_{coil} + R_S)^2}} \quad (5.3)$$

$$\angle \frac{I_S(j\omega)}{V_{coil}(j\omega)} = \tan^{-1} \left(\frac{\omega(R_{coil} + R_S)C_p}{1 - \omega^2 L_{coil} C_p} \right) - \tan^{-1} \left(\frac{\omega L_{coil}}{R_{coil} + R_S} \right) \quad (5.4)$$

From equation (5.3) when a DC signal is sent to the coil, the magnitude of the voltage-current response is dependent on the resistance alone. Hence, the resistance of the coil can be determined as:

$$R_{coil} = \frac{1}{\left| \frac{I_S(0)}{V_{coil}(0)} \right|} - R_S \quad [\Omega] \quad (5.5)$$

From equation (5.4) when the phase delay of the response is equal to -45° , the inductive and resistive impedances are equal. Hence, the inductance of the coil can be determined as:

$$L_{coil} = \frac{R_{coil} + R_S}{\omega_c} \quad [\text{H}] \quad (5.6)$$

where, ω_c [rad/s] is the signal frequency when the measured phase delay is -45° . Identification of the self-resonant frequency $\omega_{n,DC}$, and parasitic capacitance can be accomplished by connecting a large resistance in series with the deflection coil, as shown in Figure 5.9, and recording the step

response of the voltage drop across the coil, V_{coil} for a stepped input voltage, V_{in} . The frequency of the observed oscillation in V_{coil} is equal to the self-resonant frequency $\omega_{n,DC}$, and the parasitic capacitance can be evaluated from equation (3.10).

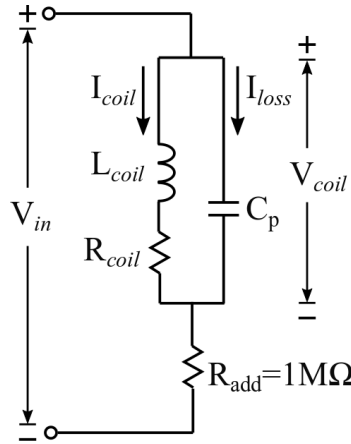


Figure 5.4: Experimental circuit for measurement of deflection coil self-resonant frequency.

5.1.2 Two-Axis Canmora EBM Machine

Experiments where the deflection of an electron beam was completed, were conducted in the Canmora EBM machine seen in Figure 5.5. The Canmora EBM is an electron beam welding machine that was retrofitted with a powder deposition system for AM. The accelerating voltage parameter, V_A , was set to 100 kV for all deflection experiments. The vacuum chamber of the Canmora EBM machine was 2.5m length x 1m width x 1.5m height and contains an x-y motion stage for positioning workpieces below the electron beam gun. The AM build plate has a 96 mm diameter was positioned 750 mm below the axis of deflection coils. The geometry and number of turns of the Canmora EBM's deflection coils are unknown. Therefore, the measured gains, $K_B K_d$, cannot be directly compared to the predicted and simulated values. However, deflection experiments may still be used to validate the linear nature of the current to deflection relationship.

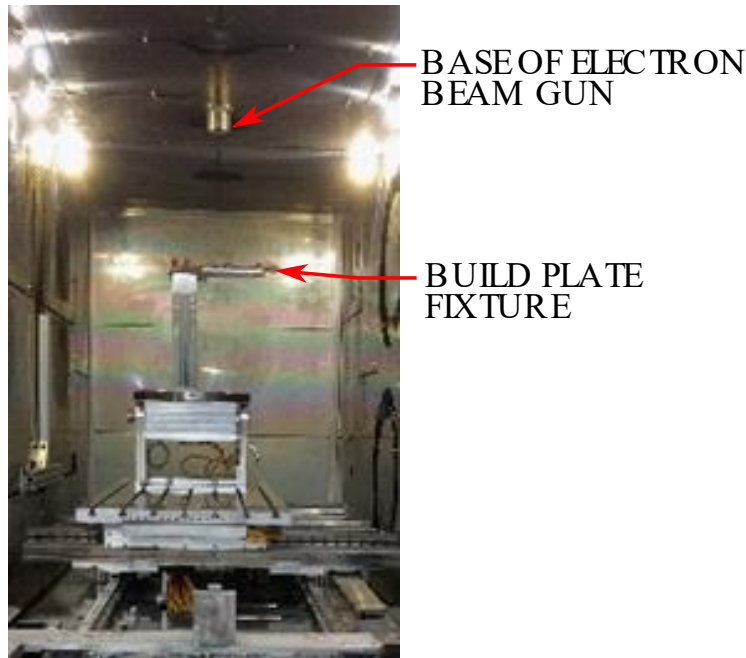


Figure 5.5: Canmora EBM machine vacuum chamber.

The current amplifier in the Canmora EBM machine is a Varedan transconductance amplifier. The current amplifier had a gain (K_{PA}) of 1 A/V, which was measured to be constant within the 1 kHz frequency range used during deflection tests. Differential voltage commands, V_{in} , are sent to the current amplifier from the Canmora EBM control computer. Prior to deflection experiments, the voltage input signal was analyzed, and excessive high frequency noise was measured (100 mV peak-to-peak noise) on the EBM computer output. To reduce the noise in the voltage signal, an analog passive first-order low pass filter was designed and implemented on the differential signal. The filter was implemented as an RC circuit, seen in Figure 5.6. The cutoff frequency of the filter was selected such that the delay for a 1kHz signal was not great enough to create instability for a closed-loop control system, while attenuating the noise adequately.

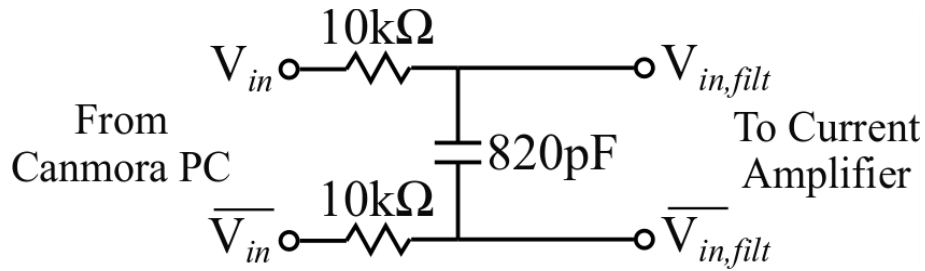


Figure 5.6: Passive low-pass filter implemented on voltage input signal.

The measured FRF of the low-pass filter can be seen in Figure 5.7, the -3dB corner frequency was measured at approximately 15 kHz. If signals of differing frequency are sent to each deflection axes, the delay induced by the filter may create a discrepancy between reference input signal and deflection output signal. Therefore, for open loop experiments, the frequency of the signal sent to each axis should be equal.

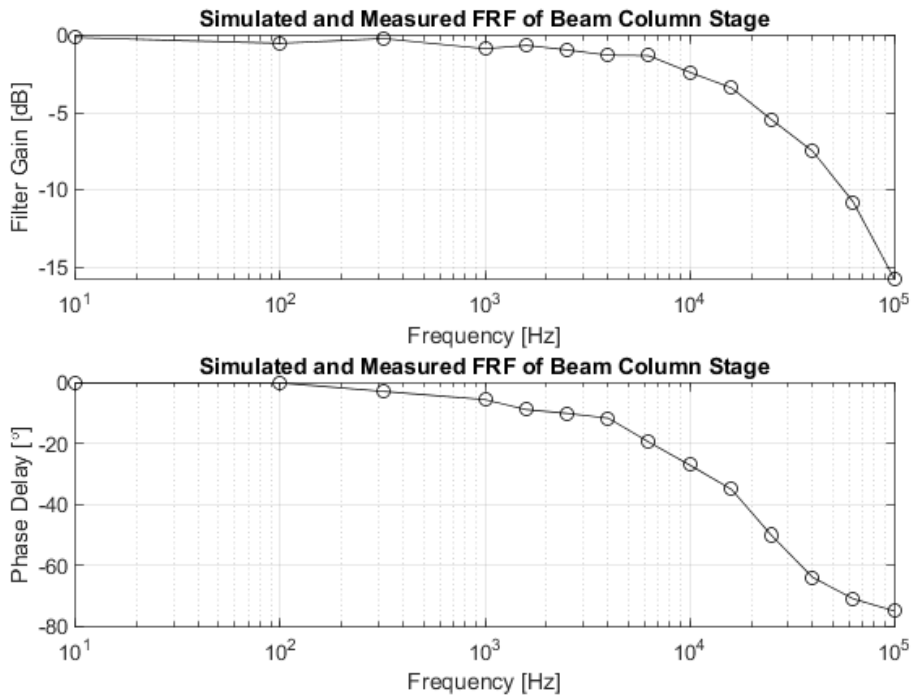


Figure 5.7: Measured FRF of voltage input filter.

For deflection experiments the voltage signal into the power amplifier, V_{in} , was measured using a dSpace 1202 Microlabbox's analog input. An electron beam was generated with 100 kV

accelerating voltage and low current and was deflected onto an aluminum 6061 build plate. The position of the beam on the build plate is measured from the resulting melt pool lines. Since the position of the melt pool is measured after the experiment is complete, the real-time position of the melt pool is not measured. As a result, any measured error in the melt pool is the contouring error rather than the tracking error, and it was not possible to measure phase delay in the output deflection during any frequency sweep experiments.

For open-loop controller testing the controllers were implemented on a dSpace 1202 MicroLabBox. The controllers were designed using Simulink software, and compiled to the dSpace real-time controller. Input voltage signals were received by the dSpace's analog inputs using coaxial cables with BNC connectors. Voltage output signals from the open-loop controllers were sent via the dSpace's analog output using coaxial cables with BNC connectors.

5.2 Results

5.2.1 Coil Voltage Response

5.2.1.1 Single-Axis Deflection System

The FRF of both the single-axis test setup's deflection coils' impedance, expressed in equation (5.2), was measured via a sinusoidal frequency sweep for input voltage (V_{coil}) for the frequency range from 0.1 Hz to 2 kHz. The input voltage signal was sent from the current control system shown in Figure 5.3, and the current in the coils was measured from the current sensing resistor, R_S . The FRF of both the deflection coils in can be seen in Figure 5.8. A first order response was observed for the swept frequency range. The DC gain of the impedance response can be approximated as the magnitude at 0.1 Hz, and the pole in the first order response was observed at

29.27 Hz. The DC-resistance, R_{coil} , and self-inductance, L_{coil} , of each coil were evaluated from equations (5.3) and (5.4), and are summarized in Table 5.1.

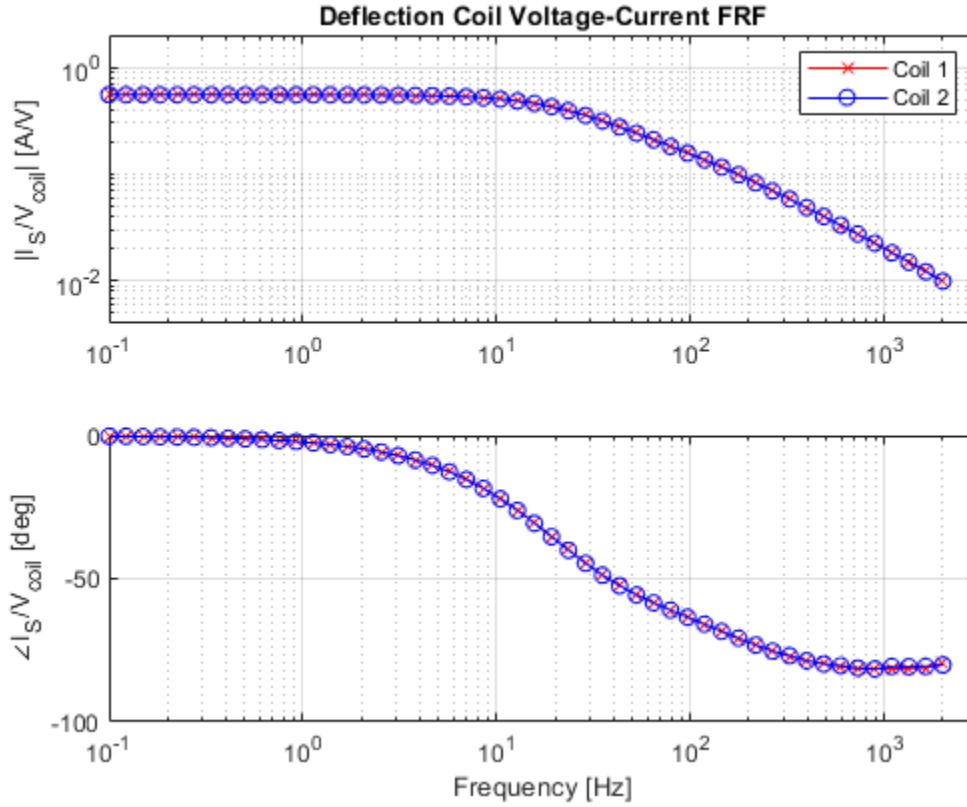


Figure 5.8: FRF of deflection coils impedance.

The self-resonant frequency, $\omega_{n,DC}$, of the single-axis test setup's deflection coils was measured using the method described in section 5.1.1.2. A stepped voltage input, V_{in} , with an amplitude of 3 V was supplied to the coil, and the recorded voltage drop across the coil, V_{coil} , is presented in Figure 5.9. The measured self-resonant frequency, $\omega_{n,DC}$, is equal to 116×10^3 rad/s (729 kHz), and the parasitic capacitance evaluated from equation (3.10) is equal to 29 pF. Since the measured self-resonant frequency is much greater than the desired operating bandwidth of the deflection system (5 kHz), the equivalent circuit of the deflection coils may be simplified to the circuit shown in Figure 3.6b, thereby simplifying the dynamics of the deflection coil stage of the deflection system

to a constant gain, $K_{B;(x,y,z)}$. Since the self-resonant frequency, $\omega_{n,DC}$, of the single-axis test setup's coils was measured to be much higher than the desired bandwidth of the deflection system ($729 \text{ kHz} \gg 5 \text{ kHz}$), the conclusion from this measurement will be applied to other deflection coils, including the deflection coils used within the Canmora EBM machine.

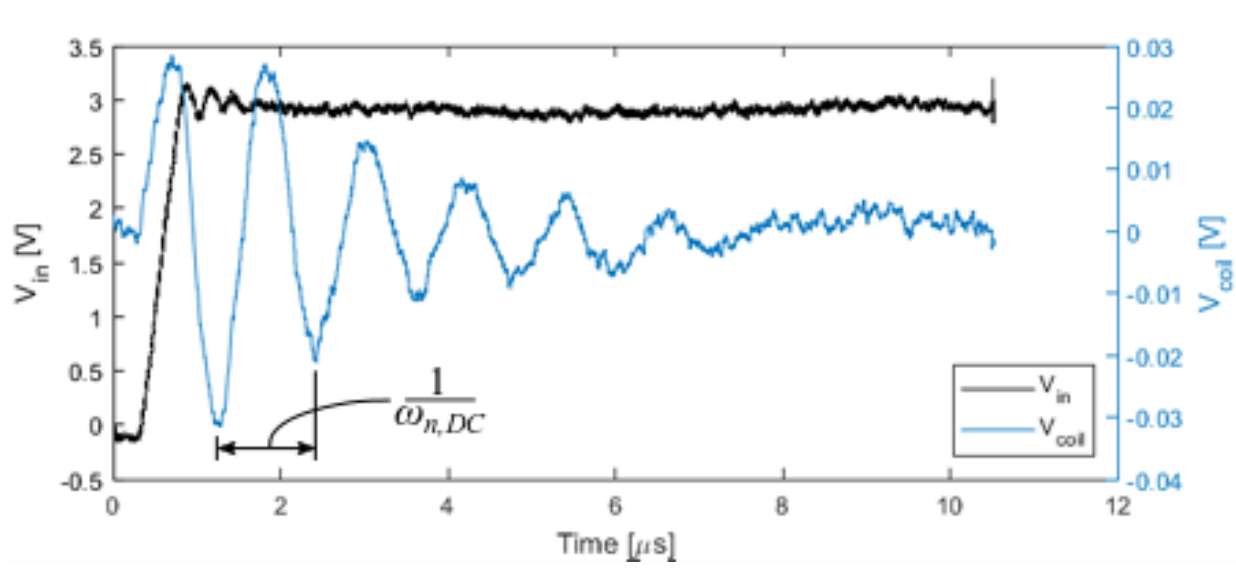


Figure 5.9: Step response of deflection coil with large resistor connected in series.

Table 5.1: Measured DC-resistance, self-inductance, and parasitic capacitance of the external deflection coils.

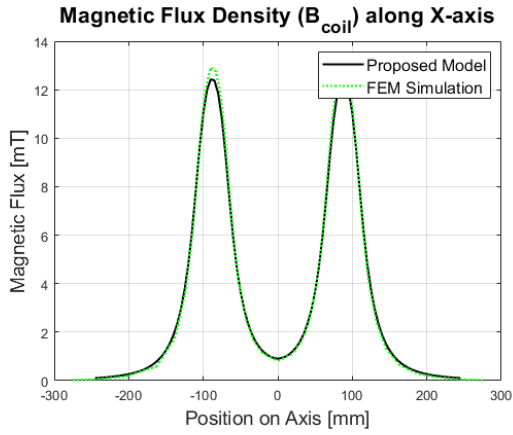
	Coil 1	Coil 2
DC-Resistance, R_{coil}	1.61 Ω	1.61 Ω
Self-Inductance, L_{coil}	9.7 mH	9.8 mH
Parasitic Capacitance, C_p	27 pF	

5.2.2 Magnetic Flux Density Distribution

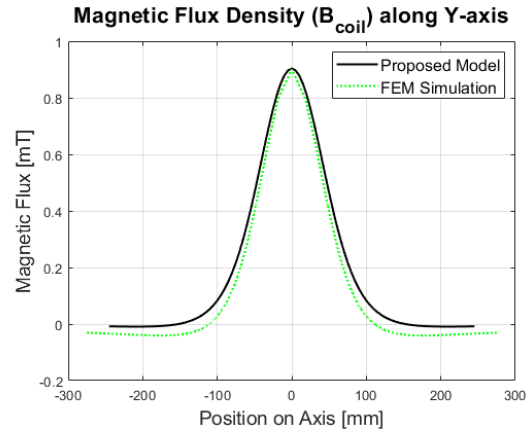
The predictive model proposed in section 3.4.2.2 of this thesis for the prediction of the magnetic flux density, B_{coil} , for a given input current, I_S , was validated with FEM simulation and measurement on the single-axis test setup.

5.2.2.1 Single-Axis Test Setup

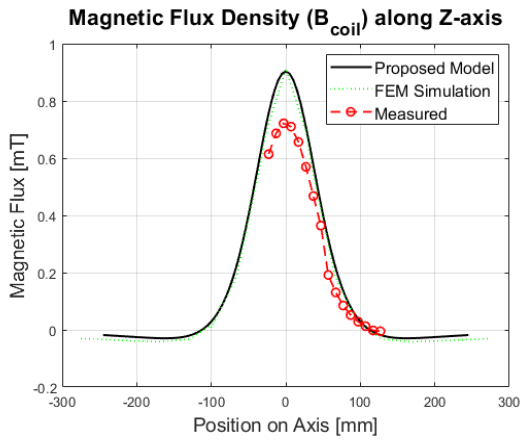
A static input current, I_S , of 1 A was supplied to the FEM modelled coils, and external single-axis deflection system. The simulated distribution of magnetic flux density output, B_{coil} , along the x-, y-, and z-axis of the deflection system was recorded. Using the adjustable leg height, the magnetic flux density was measured along the z-axis of the single-axis deflection system was measured. The FEM simulated flux density distribution ($B_{coil;(x,y,z)}$) is compared to the proposed model in Figure 5.10 where the distances are measured from the center of the deflection system. The proposed model matches the FEM simulation closely along all the system's axes. The measured flux density along the z-axis, shown in Figure 5.10c, is approximately 19% less than the predicted value at each point along the distribution. The discrepancy between the simulated and measured results is expected, as the simulated system uses ideal coils, whereas the actual coil's windings will have misalignments in the windings and coils themselves. The distributed gain $K_{B;(x,y,z)}$ of the deflection system is evaluated by dividing the computed magnetic flux, ($B_{coil;(x,y,z)}$), by the constant current, I_S , supplied to the coil, as shown in equation (3.16).



(a)



(b)



(c)

Figure 5.10: Predicted, simulated, and measured magnetic flux density distribution along system axes.

5.2.3 Beam Column Dynamic Response

The transfer function between magnetic flux density in the beam column ($B_{(x,y,z)}$) and magnetic flux generated by the deflection coils ($B_{coil;(x,y,z)}$), shown in equation (3.19), is identified using FEM simulation and validated experimentally using the external single-axis test setup and actual Canmora EBM machine .

5.2.3.1 Single-Axis Test Setup

First, the FRF of the beam column stage, shown in equation (3.20), was simulated in the frequency domain in COMSOL. Harmonic current inputs with unity amplitude ($I_s(t) = 1 \sin(2\pi ft)$) in the frequency range of 1 Hz to 10 kHz were supplied to the COMSOL simulated coils, shown in Figure 5.1. The magnitude of the flux density ($|B_{(x,y,z)}|$) at the center of the deflection system was recorded for each input frequency. The frequency domain simulation was conducted with a beam column with material properties matching aluminum 6061. Additionally, the conductivity, σ [S/m], of the beam column was varied, with all other properties held constant, such that the effect of beam column conductivity on the FRF of the system could be observed. The resulting FRFs are presented in Figure 5.11, and as expected a first order response was observed for all beam columns with a conductivity above zero, with the aluminum 6061 column response having a simulated time constant of 1.53 ms. As the conductivity, σ , of the beam column was increased, the bandwidth of the system decreased. Additionally, as the beam column conductivity increases, the amount of eddy current generated would be expected to increase, which indicates that the decrease in the FRF bandwidth is driven by an increase in eddy currents. The beam column with a conductivity approximately equal to alumina (Al_2O_3), a ceramic, showed virtually zero attenuation of magnetic flux density, $|B_{(x,y,z)}|$, for the tested frequency range. Therefore, for beam columns with very low conductivity, the response of beam column stage may be described by a unity gain component.

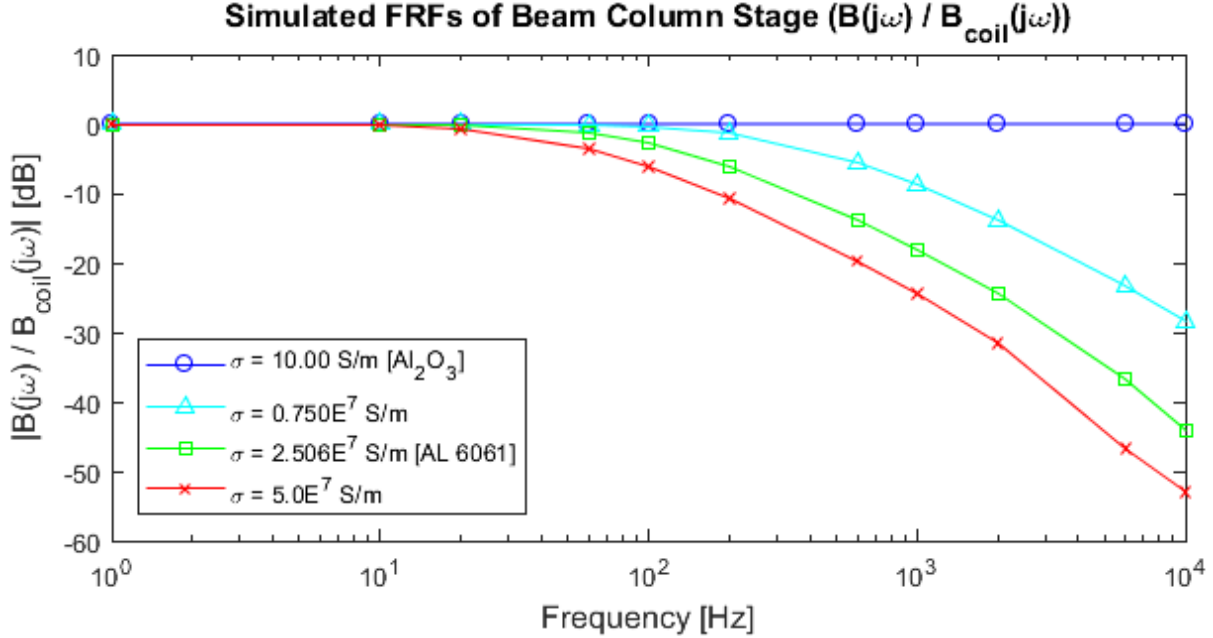


Figure 5.11: Simulated FRFs of beam column stage with various conductivities.

The FRF of beam column stage (equation (3.20)) of the deflection system was also measured experimentally with the single-axis test setup with aluminum 6061 and alumina beam columns. The single-axis coils were supplied harmonic current inputs with unity amplitude ($I_s(t) = 1 \sin(2\pi ft)$) at frequencies varying from 2 Hz to 1 kHz, and the magnitude of the magnetic flux density $|B_{(x,y,z)}|$ at the center of the system was recorded with the Gauss probe. The measured FRFs were normalized to their lowest frequency measurement, such that the gain components K_{PA} , and K_B were negated and the simulated and measured beam column stages could be compared directly, and are shown in Figure 5.12. The FEM simulated and measured FRFs match well, with a first-order response measured for the aluminum 6061 column and no attenuation in magnetic flux density was measured for the alumina beam column. The simulated beam column had a time constant of 1.53 ms, and the measured beam column had a time constant of 1.73 ms. All measured and simulated time constants for aluminum and alumina beam columns are declared in Table 5.2, along with the time constants for the two-axis Canmora EBM beam column.

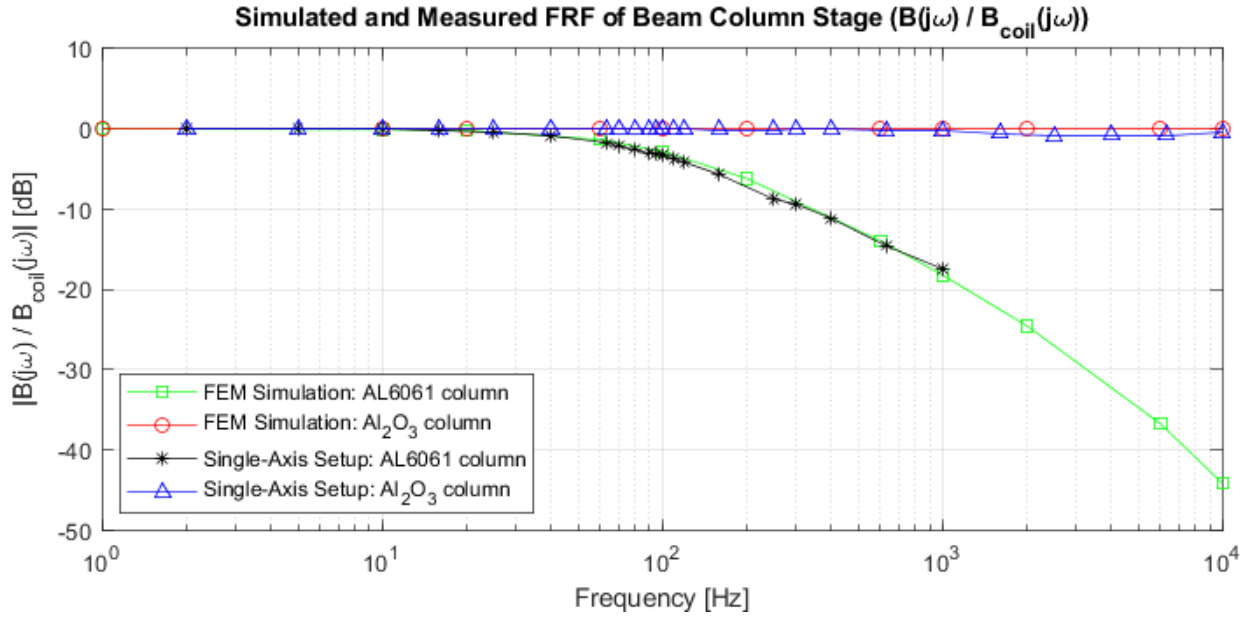


Figure 5.12: Simulated and measured FRFs of beam column stage.

5.2.3.1.1 Open-Loop Eddy Current Compensation on Single-Axis Test Setup

The effectiveness of the open-loop pole-zero cancellation controller described in section 4.1 of this thesis was tested. The controller was compiled on the dSpace 1202 MicroLabBox and was connected to the single-axis test setup with an aluminum 6061 beam column. The zero, z_c , was placed at 578 rad/s (92 Hz), and the pole, p_c , was placed at 3200 rad/s (509 Hz) to avoid saturation of the current amplifier. Harmonic current inputs ($V_{in}(t) = 1 \sin(2\pi ft)$) with a frequency range of 1 Hz to 2 kHz were sent to the coils. The magnitude of the magnetic flux density at the center of the deflection system was recorded. The resulting FRF is compared to the non-compensated FRF in Figure 5.13, and as expected a first-order response is observed. The deflection system with a pole-zero cancellation controller had a time constant of 0.259 ms, which is 1.47 ms lower than the uncompensated system. Therefore, the pole-zero cancellation controller was effective at increasing the responsivity of the electron beam deflection system.

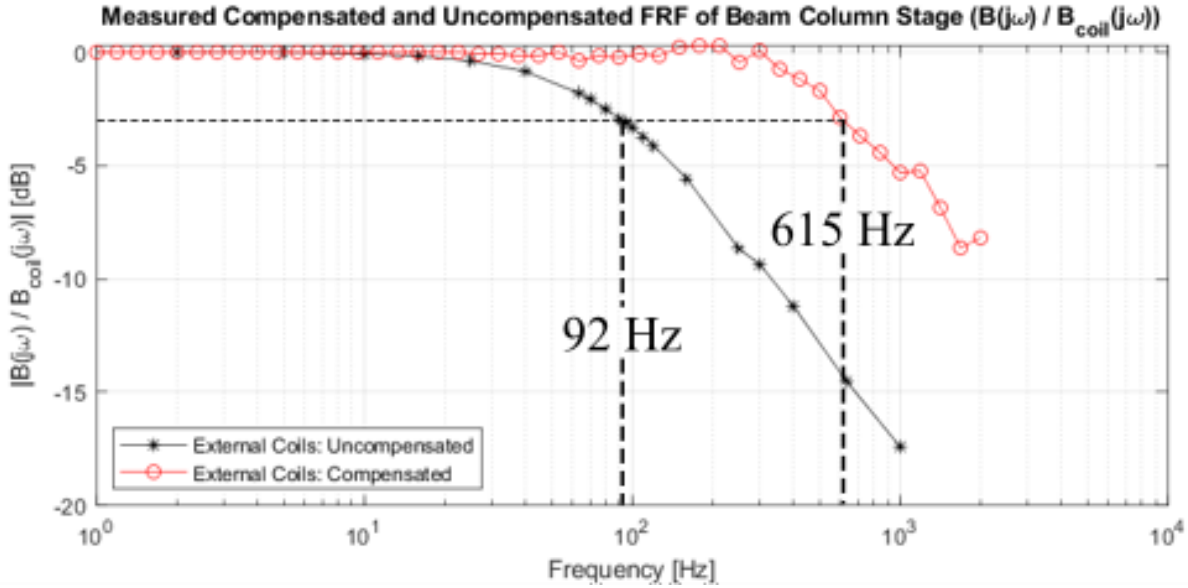
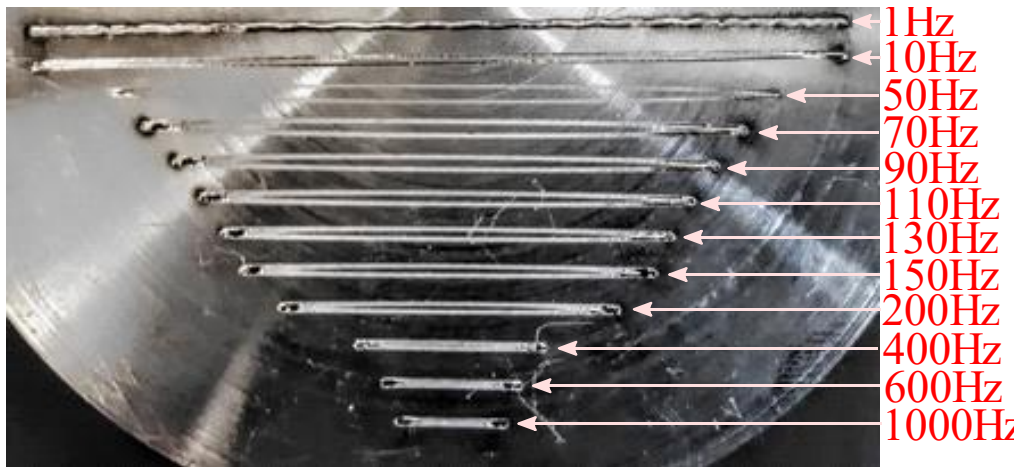


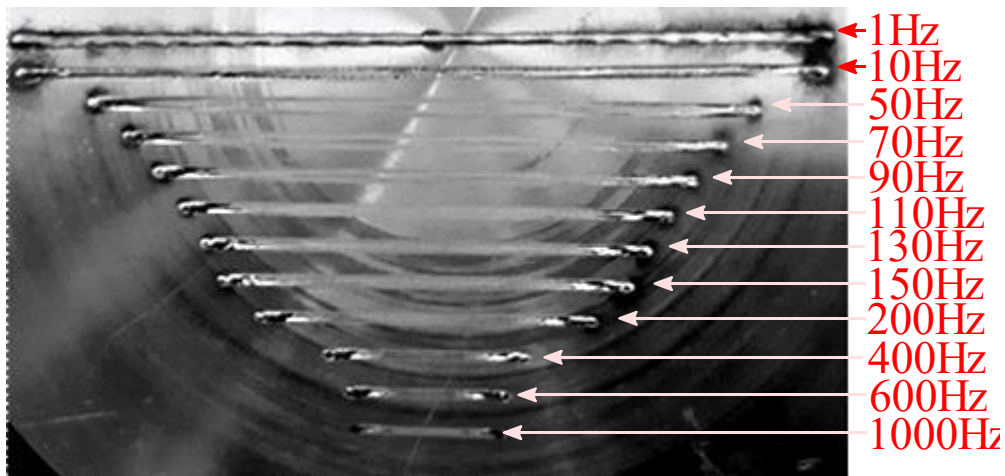
Figure 5.13: FRF of beam column stage with open-loop compensation.

5.2.3.2 Two-Axis Canmora EBM

The effects of the beam column stage were also observed in deflection experiments within the Canmora EBM. The beam column stage of the Canmora EBM machine was for each axis of the two-axis deflection measured by supplying harmonic voltage inputs with unity gain ($V_{in} = 1 \sin(2\pi ft)$) at frequencies varying from 1 Hz to 1 kHz to the a single-axis deflection system at a time and measuring the magnitude of single axis deflection output (x , or y). The resulting melt pools for the x- and y-axis are presented in Figure 5.14, the magnitude of the deflection output was measured as the length of the resulting melt pool.



(a)



(b)

Figure 5.14: Melt pools from single-axis frequency sweeps experiments. a) x-axis, b) y-axis.

The measured FRFs were normalized to their lowest frequency measurement, such that the gain components K_{pA} , K_B , and K_d were negated and the beam column stages could be compared directly, and are shown in Figure 5.15. The x-axis of the deflection system had a measured time constant of $\tau_x = 2.20$ ms, and the y-axis had a time constant of $\tau_y = 1.98$ ms. The time constants measured for the two-axis system are presented in Table 5.2, along with the simulated and measured time constants of the single-axis setup. This agreement in observed responses between

the single-axis and two-axis setups indicates that the dynamic response of the Canmora deflection system is dominated by the eddy current induced lag in the beam column, as the beam column geometry are matching between the setups.

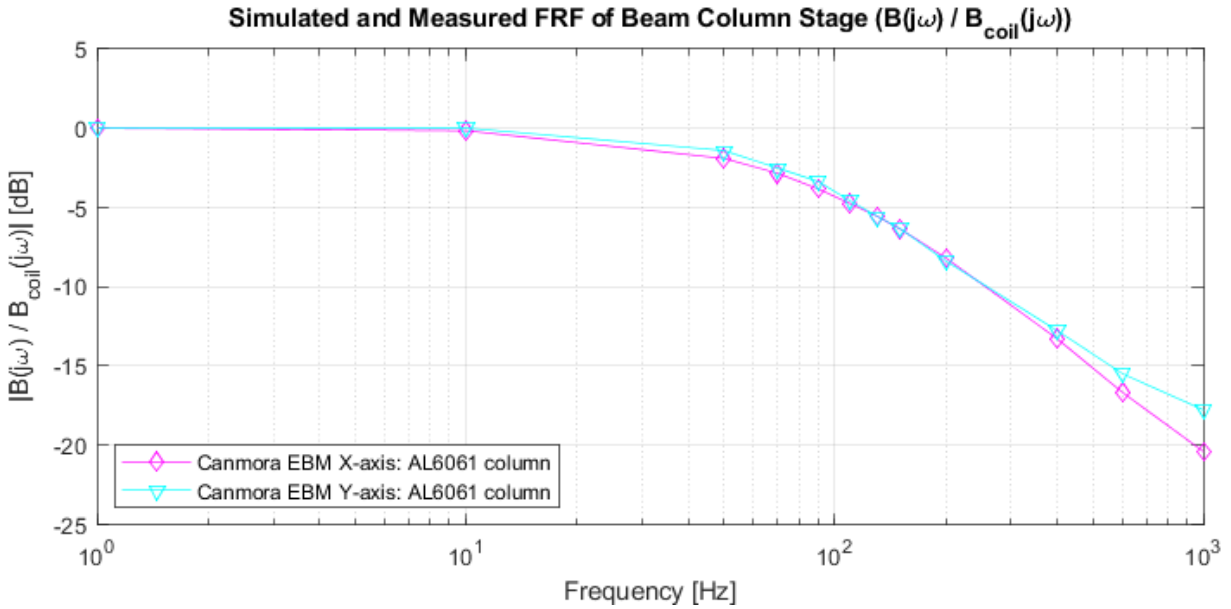


Figure 5.15: Simulated and measured FRFs of beam column stage.

Table 5.2: Summary of simulated and measured time constants of beam column stage ($B(j\omega)/B_{coil}(j\omega)$).

Beam Column Material	Aluminum 6061	Alumina (Al_2O_3)
FEM Simulation	1.53 ms	~0 ms
External Single-Axis System	1.73 ms	~0 ms
Canmora EBM X-Axis	2.20 ms	
Canmora EBM Y-Axis	1.98 ms	

5.2.4 Electron Beam Deflection

5.2.4.1 Single-Axis Deflection System

The combined gains of the deflection coil and beam deflection stages, $K_B K_d$, evaluated from the discrete-time simulation proposed in section 3.4.4 was validated via FEM simulations in COMSOL. Static input current signals, I_S , with amplitudes ranging from -0.75 A to +0.75 A were supplied to the simulated coils, and the static deflection output (y_{nom}) was recorded. The deflection output of the FEM simulation was evaluated as the particle's position 750 mm below the deflection coil axis. The accelerating voltage for all simulations was set to 100 kV. Figure 5.16 shows the plot of predicted, and COMSOL simulated deflection (y_{nom}) values against the input current (I_S), with linear relationships observed, validating the model simplification in equation (3.26). The discrete-time simulation model predicted a gain, $K_B K_d$, of 0.0510 m/A, which matched the simulated value of 0.0495 m/A closely, thereby validating the proposed model.

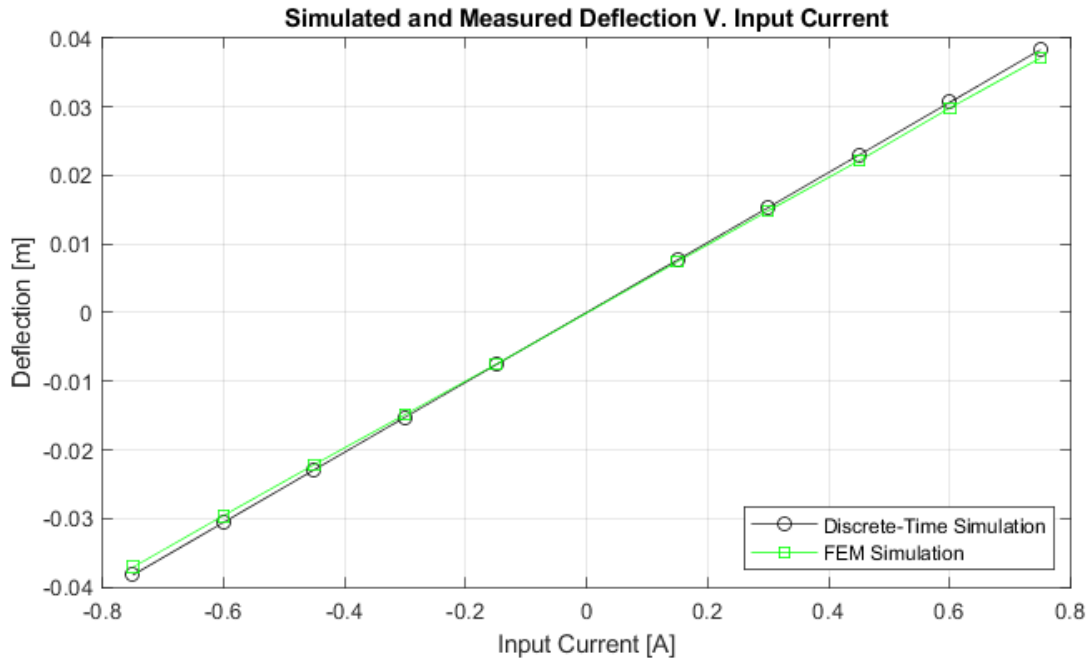


Figure 5.16: Deflection output (x , or y) for varying current input (I_S) amplitudes.

The effect of the accelerating voltage, V_A , on the deflection gain, K_d , was simulated using the discrete-time simulation proposed in section 3.4.4. The accelerating voltage was varied between 50 kV to 200 kV and the magnitude of the electron velocity (v_0), was evaluated from the equation (3.6). The beam deflection was simulated with a static current, $I_{S,x}$, with an amplitude of 1 A. The output deflection, x , was measured on a built plate 750 mm below the axis of the deflection coils and is plotted against the accelerating voltage in Figure 5.17. The output deflection for a unity input is equal to the deflection gain (i.e. $K_B K_d = x_{nom}$ for $I_S = 1$ A). The output deflection was simulated to decrease with increasing accelerating voltage, with the sensitivity to accelerating voltage decreasing with increasing accelerating voltage. Therefore, for beams with higher velocity a higher power deflection system may be required to ensure the beam can be deflected over the entire area of the build plate.

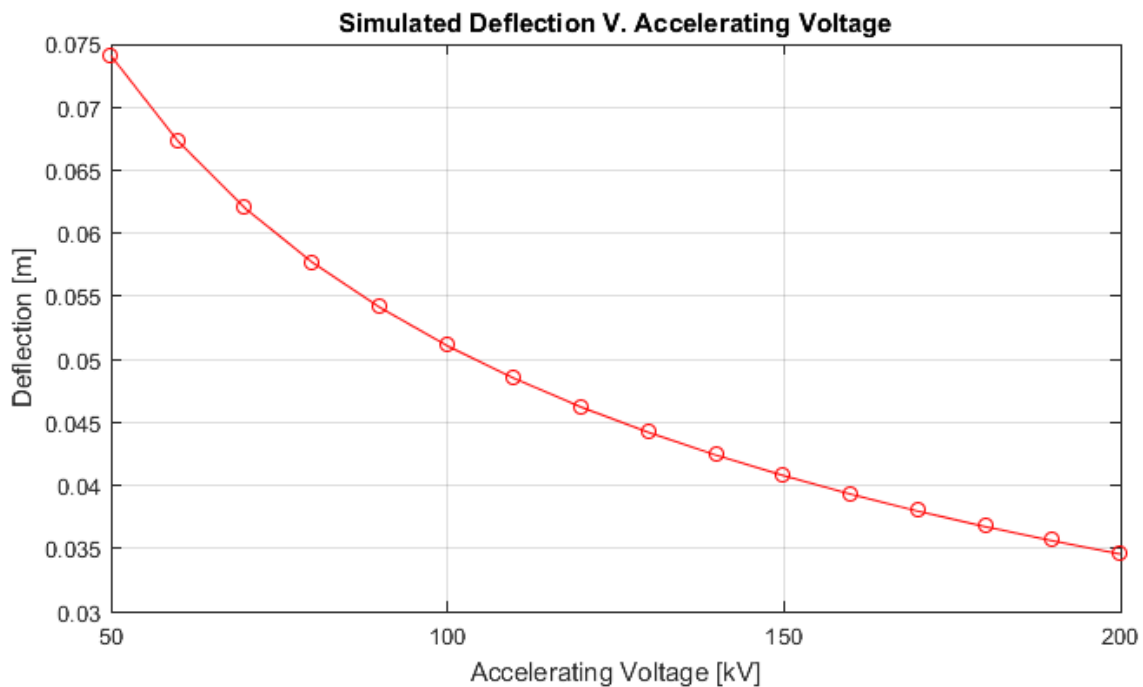


Figure 5.17: Deflection output (x_{nom}) for varying accelerating voltages (V_A).

5.2.4.2 Two-Axis Canmora EBM

Static input current signals, I_S , with amplitudes ranging from -1 A to +1 A were supplied to the Canmora EBM deflection coils, and the static deflection output (x_{nom} , or y_{nom}) was measured from the position of the resulting static melt pool on an aluminum build plate (shown in Figure 5.18).

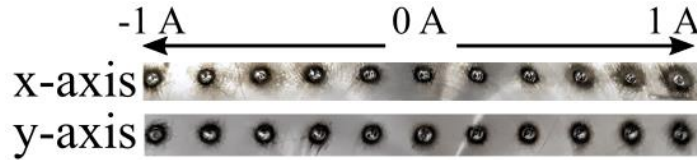


Figure 5.18: Melt pools from static currents of $I_S = -1\text{A}$ to $I_S = 1\text{A}$.

An accelerating voltage of 100 kV was used during all deflection experiments. Figure 5.19 shows the plot of measured deflection (x_{nom} , or y_{nom}) values against the input current (I_S), with linear relationships observed for both axes of the system, again validating the model simplification in equation (3.26). As mentioned in section 5.1.2, the geometry and winding specifications of the Canmora EBM is unknown, so measured deflection is not directly comparable to the proposed model or FEM simulation. The gain, $K_B K_d$, of the Canmora deflection system was measured to be 0.0335 m/A in the x-axis and 0.0341 m/A in the y-axis.

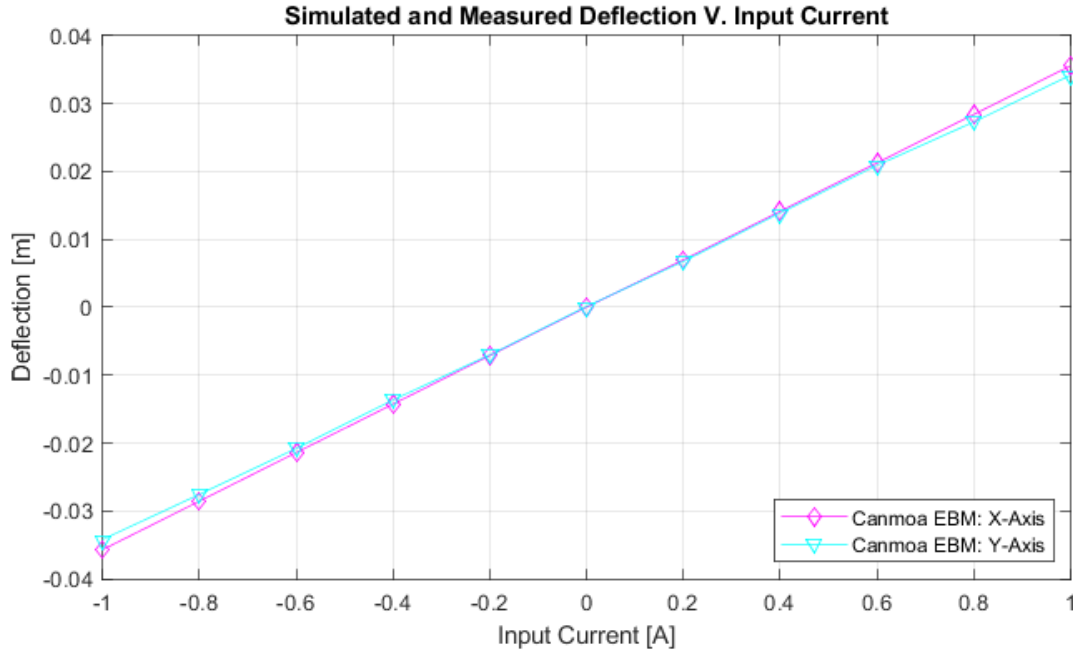


Figure 5.19: Deflection output (x , or y) for varying current input (I_s) amplitudes.

5.2.5 Crosstalk Response and Compensation

5.2.5.1 Two-Axis Canmora EBM

The effect of crosstalk between deflection coil axes was measured in the Canmora EBM machine. The crosstalk parameters α_{CT} , and τ_{CT} were identified from non-compensated frequency sweep and angular sweep of the Canmora deflection system. The frequency sweep described in section 5.2.3, and shown in Figure 5.14 were used to identify the crosstalk parameters. The angular sweep was completed by sending harmonic signals with a frequency of 50 Hz to both axis simultaneously with a scaling factor applied to the input signals to change the angle of the beam velocity (i.e. $V_{in,x} = \text{triangle}(100\pi t)\cos(\phi)$, and $V_{in,y} = \text{triangle}(100\pi t)\sin(\phi)$, where ϕ is the angle of beam velocity in radians). The angle of velocity, ϕ , was varied from 0 radians to $7/8\pi$ radians by $1/8\pi$ radian steps. The output beam position (x, y) was measured from the resulting melt pool seen in Figure 5.20. The crosstalk observed in the single-axis frequency sweep shows an initial increase

of crosstalk with frequency, followed by a decrease of crosstalk after the 50 Hz measurement. The eddy currents in the beam column signals that attenuate signals with frequencies greater than 92 Hz, as shown in Figure 5.15, and the pole in the crosstalk model occurs near 50 Hz, thereby causing the crosstalk magnitude to decrease as the two-poles dominate the zero in the crosstalk model. The angular sweep of the deflection system shows nearly zero crosstalk when the input for each axis was identical ($\phi = 2\pi/8$), with the crosstalk increasing as the voltage difference across the coils increases. The maximum crosstalk was observed when the input signals are inverted ($V_{in,x} = -V_{in,y}$, and $\phi = 6\pi/8$).

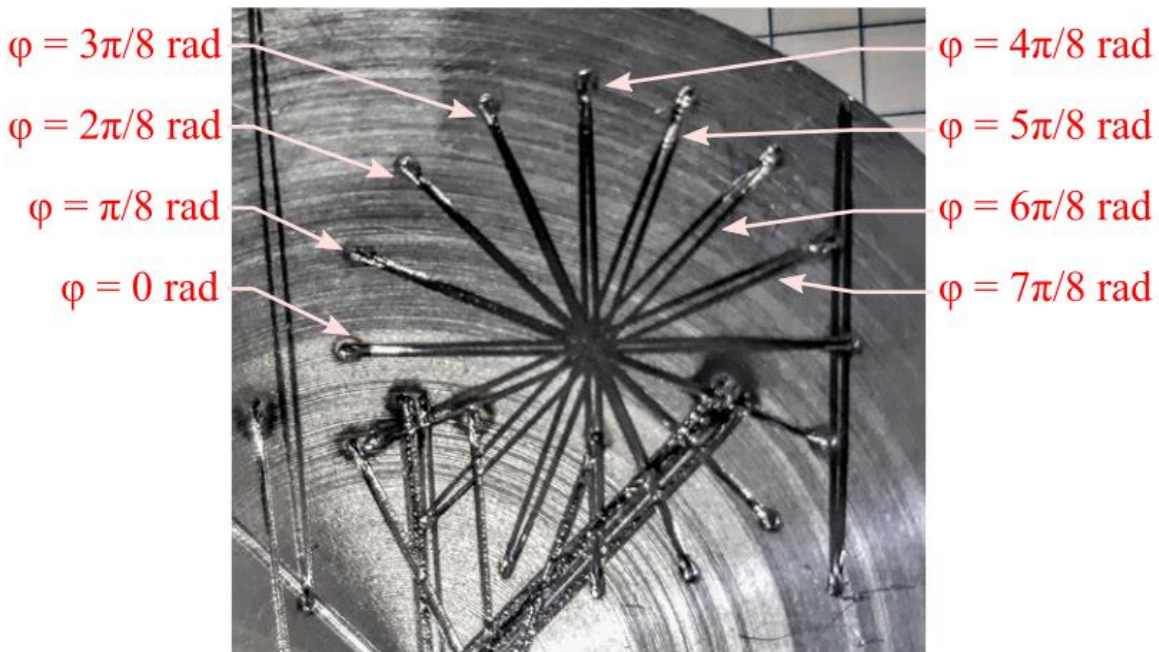


Figure 5.20: Resulting melt pool from angular sweep of Canmora deflection system.

A Simulink model of the deflection system was generated using the empirical models and the identified parameters. The Simulink model can be seen in Figure 5.21. The inputs into the Simulink model were harmonic voltage inputs, identical to the inputs used during the experimental frequency and angular sweeps on the Canmora EBM. The simulated beam positions were plotted

and are shown in Figure 5.22. The crosstalk model parameters were varied until the simulated and experimental melt pools matched well. The simulated and experimental models match well when compared visually, indicating that the model is a good predictor of axes crosstalk. From the crosstalk results values of $\alpha_{CT} = 1.5 \times 10^{-4}$ and $\tau_{CT} = 3.5 \times 10^{-3}$ could be identified.

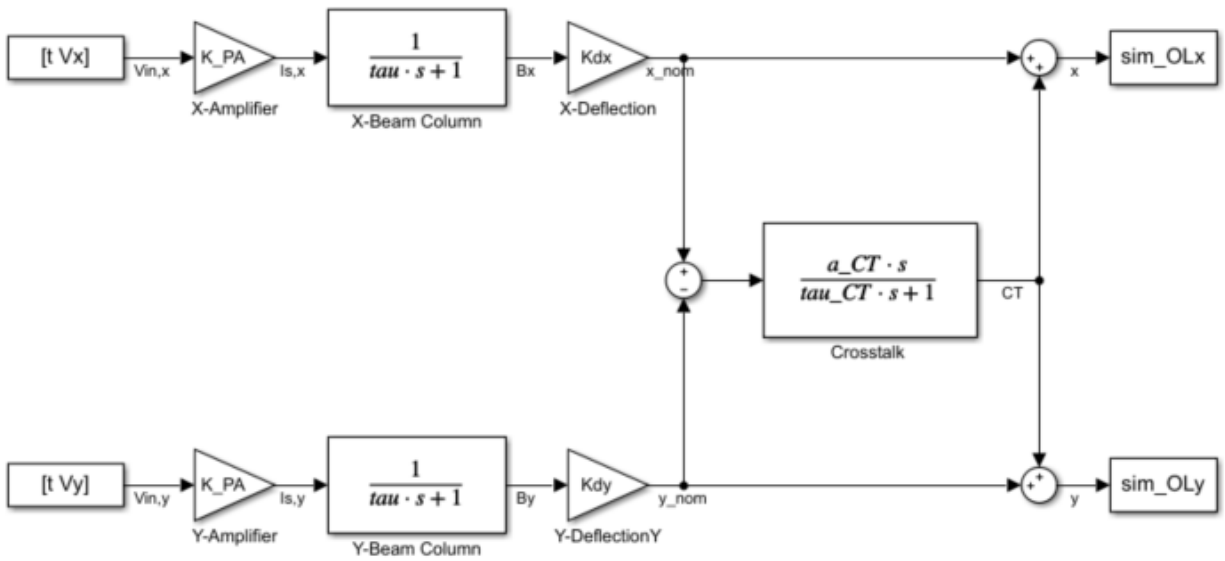
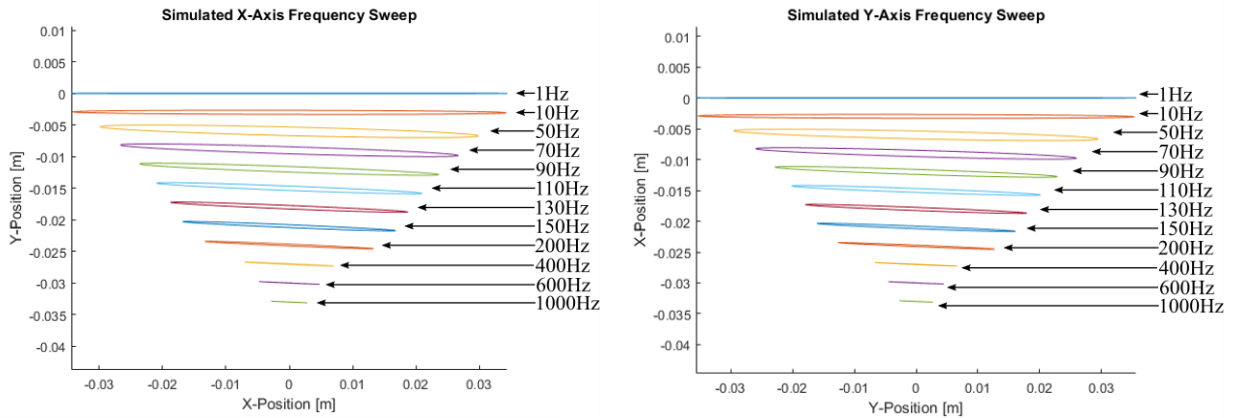
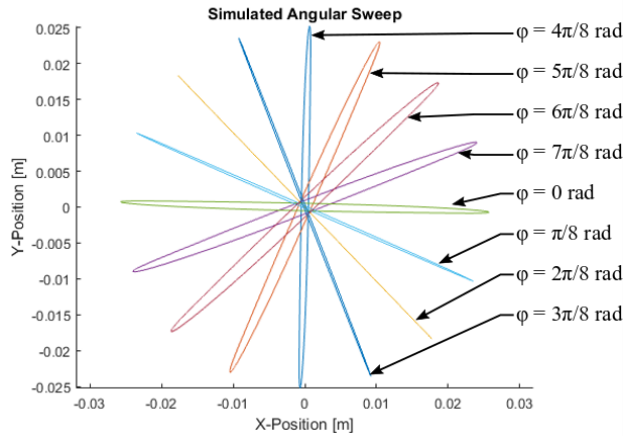


Figure 5.21: Simulink model of electron beam deflection system, used for calibration of crosstalk parameters.



(a)

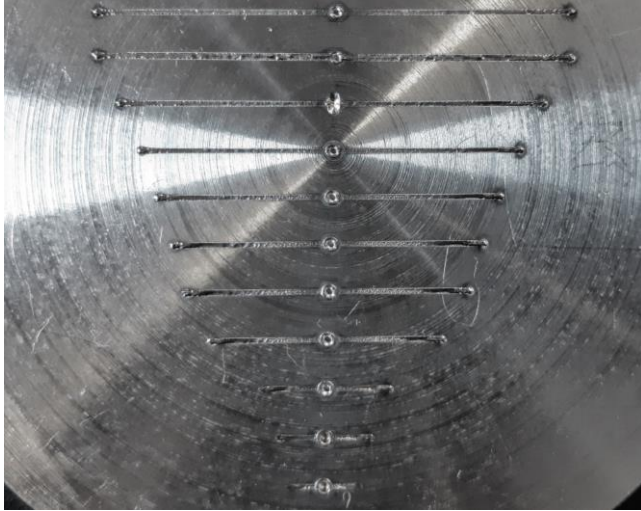
(b)



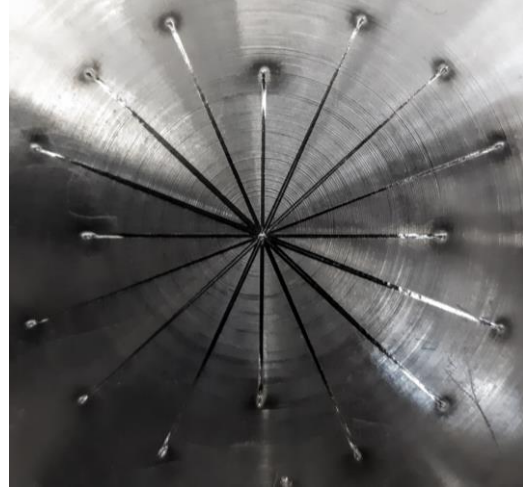
(c)

Figure 5.22: Output of Simulink simulated open-loop deflection system a) x-axis frequency sweep, b) y-axis frequency sweep, c) two-axis angular sweep

The crosstalk model was then used to implement a feed forward crosstalk compensation controller as described in section 4.2 of this thesis. Identical frequency and angular sweeps were conducted with the feed forward controller providing compensation signals to the current amplifier. The compensated melt pools can be seen in Figure 5.22. The feed forward controller was effective at removing the crosstalk from the single-axis frequency sweep, and nearly all of the crosstalk from the angular sweep. A small amount of crosstalk was remaining in the compensated angular sweep, with the largest remaining crosstalk occurring for in phase input signals. This remaining crosstalk indicates there are uncaptured dynamics within the crosstalk model and further development and tuning should be conducted to increase the effectiveness of the feed forward compensation controller.



(a)



(b)

Figure 5.23: Experimental output for beam deflection system with feed forward compensation of crosstalk. a) x-axis frequency sweep, b) two-axis angular sweep

5.3 Summary

The model of an electron beam deflection system presented in Section 3.4 of this thesis was validated and parameters within the model were identified via FEM simulation, Simulink simulation, and experimentation. From the measured FRF of the deflection coils' impedance, and measurement of the coils' parasitic capacitance, the current behavior within the deflection may be simplified to a unity constant gain as shown in (3.11). The deflection systems current to magnetic flux density distribution was mapped along the Cartesian directions, with the FEM simulations and proposed model matching very well, and the measured response within 13% of the predicted magnetic flux distribution. The dynamic response of the beam column stage was simulated and measured to be first-order as described in equation (3.19), with the time constant of the response being dependent on the conductivity of the beam column. The linearity of deflection system's current to deflection response was validated, with the deflection gains, $K_{d,x}$ and $K_{d,y}$, identified.

Simulation of beam deflection demonstrates that increasing the accelerating voltage, V_A , within the electron gun, decreases the beam deflection for a given input current, I_S . The measured response of the deflection system may be represented by the simplified block diagram in Figure 5.24.

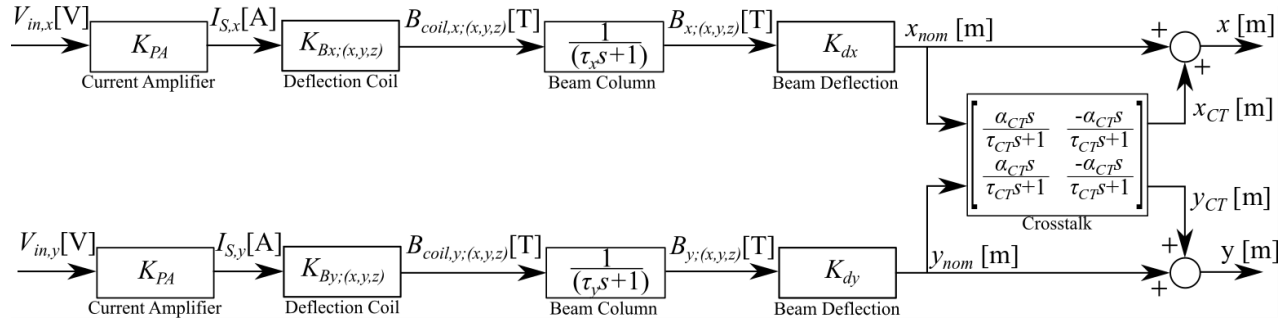


Figure 5.24: Simplified block diagram of deflection system representing the measured response.

The eddy current induced lag was compensated for with a pole-zero cancellation controller, with a decrease of the deflection system's time constant from 1.53ms to 0.259ms. However, the response of an alumina (Al_2O_3) beam column was measured to have a time constant of approximately zero. Therefore, to increase the responsivity of the deflection system it is recommended that the aluminum 6061 beam column is replaced by an alumina or similarly nonconductive material beam column.

A feed forward crosstalk compensation controller was tested and was able to significantly reduce the beam position error caused by crosstalk between the system's axes. Further tuning of the crosstalk model is required to reduce the crosstalk induced error to zero.

Chapter 6: Conclusion

A model of the electron beam deflection system that predicts the position of the electron beam on the build plate from system inputs is presented. Validation of the model was completed through FEM simulations and experimentation on two separate experimental setups, including a novel single-axis deflection system. Prediction of the magnetic flux density distribution generated by the coils in the deflection system was completed and validated through FEM simulation and experimentation. The distribution of magnetic flux density was used to predict the deflection of the electron beam. The position on the build plate was shown to have a linear relationship with the current in the deflection coils, such that the beam deflection stage of the deflection system may be modelled as a constant gain component. The dynamics of electron beam deflection system was shown to be dominated by the lag induced by eddy currents within the conductive beam column. The time constant of the beam column stage was shown through FEM simulation to be dependent on the conductivity of the beam column material, with higher conductivity beam columns having a larger time constant (i.e. increasing conductivity in the beam column decreases the system's responsivity). A nonconductive ceramic beam column was simulated and measured to remove the eddy current induced lag. An empirical model of crosstalk was fitted to two-axis deflection experiments within the Canmora EBM machine.

With the presented model, open-loop control strategies were implemented to compensate for the errors induced by eddy current in the beam column and crosstalk between the system's axes. A pole-zero cancellation controller was used to increase the bandwidth of the deflection system. The pole-zero cancellation controller predicted the lag induced by the eddy currents within the beam

column and amplified the input signal to compensate. The pole-zero cancelation controller was demonstrated on a single-axis deflection test setup to decrease the time constant of the deflection system from 1.73 ms, to 0.259 ms. A feed forward controller was designed, which used the model for crosstalk to compensate for errors induced by crosstalk in real-time. The designed controller was effective in removing most of the crosstalk induced error in the Canmora EBM beam's position. The remaining error may be caused by uncaptured dynamics in the empirical model or mistuning of the crosstalk parameters. Although both open-loop control techniques demonstrated effectiveness in compensating for errors in the electron beam deflection system, both controllers are not robust and rely heavily on accurate models for successful implementation.

With the material presented in this thesis, it is possible to develop an electron beam deflection system that would have a very high bandwidth and would produce small errors in the electron beam's trajectory on the build plate. As highlighted in this thesis, alterations to some of the hardware in the electron beam gun can greatly increase the system's bandwidth and decrease crosstalk between axes. Replacing the conductive beam column with a nonconductive beam column would remove the eddy current induced lag, increasing the system's bandwidth to the bandwidth of the next slowest stage, likely the current amplifier.

6.1 Future Directions

The next step recommended by this thesis is to implement a closed-loop control system for beam position control on an EBM machine. As shown in this thesis the magnetic flux density within the beam column is a state, which may provide information on the position of the electron beam on the build plate. Measurement of the magnetic flux density within the beam column may be

accomplished with a high bandwidth hall probe or magnetometer. Further experiments should be conducted to measure the magnetic flux density within a two-axis electron beam deflection system to observe the magnetic flux density's crosstalk response. If the crosstalk between the axes of the system can be measured in the magnetic flux density within the beam column, it may be possible to achieve closed-loop control of the beam's position on the build plate. To achieve closed-loop control the measurement of magnetic flux density within the beam column should be fed into an observer (e.g. Kalman filter) to estimate the beam's position in real-time. Closed-loop control would provide a more robust solution than the open-loop control strategies presented in this thesis.

With more robust control of the electron beam's position on the build plate, further investigation into the control and optimization of the EBM process can be undertaken. Optimization of the beam's trajectory during part production may be allow for a more even and consistent part temperature, thereby reducing internal stresses within the part and reducing the likelihood of part defects, such as porosity, which may degrade the finished part's mechanical properties.

Bibliography

- [1] M. Vaezi, S. Chianrabutra, B. Mellor, and S. Yang, “Multiple material additive manufacturing – Part 1: a review,” *Virtual Phys. Prototyp.*, vol. 8, no. 1, pp. 19–50, Mar. 2013, doi: 10.1080/17452759.2013.778175.
- [2] S. P. Narra, R. Cunningham, J. Beuth, and A. D. Rollett, “Location specific solidification microstructure control in electron beam melting of Ti-6Al-4V,” *Addit. Manuf.*, vol. 19, pp. 160–166, Jan. 2018, doi: 10.1016/j.addma.2017.10.003.
- [3] Bai *et al.*, “Additive Manufacturing of Customized Metallic Orthopedic Implants: Materials, Structures, and Surface Modifications,” *Metals*, vol. 9, no. 9, p. 1004, Sep. 2019, doi: 10.3390/met9091004.
- [4] S. Liu and Y. C. Shin, “Additive manufacturing of Ti6Al4V alloy: A review,” *Mater. Des.*, vol. 164, p. 107552, Feb. 2019, doi: 10.1016/j.matdes.2018.107552.
- [5] Z. Cordero, H. Meyer III, P. Nandwana, and R. Dehoff, “Powder bed charging during electron-beam additive manufacturing,” *Acta Mater.*, vol. 124, Feb. 2017, doi: 10.1016/j.actamat.2016.11.012.
- [6] S. Tammas-Williams, H. Zhao, F. Léonard, F. Derguti, I. Todd, and P. B. Prangnell, “XCT analysis of the influence of melt strategies on defect population in Ti–6Al–4V components manufactured by Selective Electron Beam Melting,” *Mater. Charact.*, vol. 102, pp. 47–61, Apr. 2015, doi: 10.1016/j.matchar.2015.02.008.
- [7] P. Edwards, A. O’Conner, and M. Ramulu, “Electron Beam Additive Manufacturing of Titanium Components: Properties and Performance,” *J. Manuf. Sci. Eng.*, vol. 135, no. 6, p. 061016, Dec. 2013, doi: 10.1115/1.4025773.

- [8] S. S. Al-Bermani, M. L. Blackmore, W. Zhang, and I. Todd, "The Origin of Microstructural Diversity, Texture, and Mechanical Properties in Electron Beam Melted Ti-6Al-4V," *Metall. Mater. Trans. A*, vol. 41, no. 13, pp. 3422–3434, Dec. 2010, doi: 10.1007/s11661-010-0397-x.
- [9] C. J. Smith *et al.*, "Dimensional accuracy of Electron Beam Melting (EBM) additive manufacture with regard to weight optimized truss structures," *J. Mater. Process. Technol.*, vol. 229, pp. 128–138, Mar. 2016, doi: 10.1016/j.jmatprotec.2015.08.028.
- [10] N. Béraud, F. Vignat, F. Villeneuve, and R. Dendievel, "Improving dimensional accuracy in EBM using beam characterization and trajectory optimization," *Addit. Manuf.*, vol. 14, pp. 1–6, Mar. 2017, doi: 10.1016/j.addma.2016.12.002.
- [11] S. E. Oltean and M. Abrudean, "Advanced Control of the Electron Beam Welding," *Control Eng. Appl. Inform.*, vol. 10, no. 1, pp. 40–48, Mar. 2008.
- [12] S. E. Oltean and M. Abrudean, "3D Control System of the Electron Beam Spot," in *2008 IEEE International Conference on Automation, Quality and Testing, Robotics*, Cluj-Napoca, 2008, vol. 2, pp. 85–90, doi: 10.1109/AQTR.2008.4588799.
- [13] S.-E. Oltean and M. Dulău, "Focusing and Deflecting Systems Modelling and Simulation of the Electron Beam Equipment CTW 5/60," in *Proceedings of the InterEng 2009*, Tirgu-Mures, 2009, pp. 138–143.
- [14] J. T. L. Thong and F. Li, "High-speed operation of scanning electron microscope lenses," *Scanning*, vol. 19, no. 4, pp. 275–280, Dec. 1996, doi: 10.1002/sca.4950190405.
- [15] K. W. Lee and J. T. L. Thong, "Improving the speed of scanning electron microscope deflection systems," *Meas. Sci. Technol.*, vol. 10, no. 11, pp. 1070–1074, Nov. 1999, doi: 10.1088/0957-0233/10/11/316.

- [16] J. T. L. Thong and B. C. Breton, “Improving the dynamic response of magnetic electron lens,” *Meas. Sci. Technol.*, vol. 2, pp. 1116–1118, 1991.
- [17] R. Nishi, N. Matsuo, and A. Takaoka, “Measurement and analysis of dynamic response of massive magnetic electron lenses,” *Meas. Sci. Technol.*, vol. 7, no. 8, pp. 1124–1127, Aug. 1996, doi: 10.1088/0957-0233/7/8/006.
- [18] D. C. Flugan, “Nuclear Magnetic Resonance Eddy Field Suppression Apparatus,” US4585995, 1986.
- [19] S. Bajekal, A. Joo Kim, M. G. Vrazel, and C. Summers, “Method and System for Crosstalk Cancellation,” US7050388B2, 2006.
- [20] H. Schultz, *Electron Beam Welding*. Abington, England: Abington Publishing, 1993.
- [21] P. W. Hawkes, “Aberration correction past and present,” *Philos. Trans. R. Soc. Math. Phys. Eng. Sci.*, vol. 367, no. 1903, pp. 3637–3664, Sep. 2009, doi: 10.1098/rsta.2009.0004.
- [22] A. Azhirnian and D. Svensson, “Modeling and Analysis of Aberrations in Electron Beam Melting (EBM) Systems,” Chalmers University of Technology, Gothenburg, Sweden, 2017.
- [23] F. Terman, *Radio Engineers Handbook*. McGraw-Hill Book Company Inc., 1943.
- [24] D. K. Cheng, *Field and wave electromagnetics*. Reading, Mass: Addison Wesley, 1983.
- [25] W. Smythe, *Static and Dynamic Electricity*, 3rd ed. USA: Taylor and Francis, 1989.
- [26] M. J. Dekker, “Eddy currents induced by deflection fields in electron guns of cathode ray tubes,” *IEEE Trans. Magn.*, vol. 33, no. 2, pp. 2179–2182, Mar. 1997, doi: 10.1109/20.582764.
- [27] R. Egerton, *Physical principles of electron microscopy*. New York, NY: Springer Berlin Heidelberg, 2016.
- [28] “AC/DC Module Application Library Manual.” COMSOL Multiphysics, 2015.